Data-Driven Robust State Estimation for Reduced-Order Models of 2D Boussinesq Equations with Parametric Uncertainties

Benosman, Mouhacine; Borggaard, Jeff

Abstract

A robust, low-order POD-based state estimator, also known as an observer, for the challenging fluid-dynamics test-case of uncertain 2D Boussinesq equations is presented in this paper. The observer design is based on the methodology recently introduced by the authors1, which incorporates robustness to bounded model uncertainties, and data-driven auto-tuning of the observer gains. An extensive numerical study on the 2D Boussinesq equations with parametric uncertainties demonstrates the performance of our observer. The reported numerical results show that the proposed observer allows estimation of the complete temperature and velocity fields from a reduced number of measurements. It is also shown that the proposed observer is robust to changes or errors in the value of the Reynolds number. In other words, we show that we can design the observer based

Data-Driven Robust State Estimation for Reduced-Order Models of 2D Boussinesq Equations with Parametric Uncertainties

Mouhacine Benosman[*], Jeff Borggaard [†]

October 15, 2020

Abstract

A robust, low-order POD-based state estimator, also known as an observer, for the challenging fluid-dynamics test-case of uncertain 2D Boussinesq equations is presented in this paper. The observer design is based on the methodology recently introduced by the authors[1], which incorporates robustness to bounded model uncertainties, and data-driven auto-tuning of the observer gains. An extensive numerical study on *the 2D Boussinesq equations with parametric uncertainties* demonstrates the performance of our observer. The reported numerical results show that the proposed observer allows estimation of the complete temperature and velocity fields from a reduced number of measurements. It is also shown that the proposed observer is robust to changes or errors in the value of the Reynolds number. In other words, we show that we can design the observer based

---

[*]M. Benosman (corresponding author: m_benosman@ieee.org) is with Mitsubishi Electric Research Laboratories (MERL), Cambridge, MA 02139, USA.

[†]Jeff Borggaard is with the Department of Mathematics and the Interdisciplinary Center for Applied Mathematics, Virginia Tech, Blacksburg, VA 24061, USA.

[1]In [1] the authors introduced the methodology on an academic example, in the form of a 1D Burgers equation. This paper on the other hand focuses on the application of this methodology to a challenging thermo-fluid test-case, in the form of 2D Boussinesq equations.

on an assumed uncertain value for the Reynolds number, and be able to estimate the temperature and velocity solutions corresponding to actual Reynolds number.

Keywords– Thermo-fluid flow state estimation, 2D Boussinesq equations, uncertain Reynolds number, reduced-order models, POD, robustness, data-driven learning, extremum-seeking application.

1 Introduction

An important problem in heating, ventilation, and air conditioning (HVAC) management is the estimation of the entire spatially distributed airflow and temperature profiles using a limited number of optimally located sensors placed throughout a room. This problem is more generally known as observer design, where a dynamical system, often mimicking the observed system dynamics, is designed to estimate in real-time all the states of the system, from a limited number of measurements.

Due to the complexity of the partial differential equations (PDEs) that model indoor airflow and temperature, the observer design problem is challenging in this case. Indeed, two well-known PDE models that describe these systems are the Navier-Stokes (NS) equations for airflow, and the Boussinesq equations for the coupled airflow and temperature model. Several observers have been proposed for the NS equation, e.g., [2–7]. For the Boussinesq equation far fewer estimation results are available due to the nonlinear coupling between the NS equation and the energy equation, e.g., [11, 12]. Furthermore, this estimation problem is rendered even more complex when one considers model uncertainties, which are ubiquitous in real-life applications.

Indeed, there are many works that utilize adaptive control to design observers for PDE systems, where both system states and parametric uncertainties are estimated, see e.g., [8] and references therein. However, the results are often limited to linear or semi-linear PDEs with linear parametric uncertainty.

Compared to adaptive control, fewer works consider passive robust control

2

to design observers for PDEs in the presence of parametric model uncertainties. For instance, in [9], the authors consider the case of a PDE with a quadratic nonlinearity where the states and measurements are subject to time-varying disturbances, with a numerical validation of the observer on the 1D Burgers equation, without temperature equation. In [10], the authors study the problem of stabilization and observer design for the 1D heat equation with boundary uncertainty and external disturbance. They propose a two-stage unknown input observer to first estimate the uncertainty term and then observe the system states. In the recent paper [7] the authors propose to use machine learning in the form of deep neural networks to infer the relationship between sparse measurements and full states of the system. They test their methodology on the NS equations modeling a two-dimensional flow over a plate. Although, the work is an interesting perspective on using machine learning for fluid dynamics modeling, this approach intrinsically inherits the weak robustness characteristics of deep neural networks, since based on offline data collection and training, and thus has no theoretical robustness guarantees w.r.t. initial conditions errors or experimental conditions mismatches, e.g., changes of the Reynolds number.

These results are interesting but they do not tackle the challenging case of airflow and temperature estimation for the Boussinesq equations, for which there are very few available results.

In [11], the authors studied the problem of designing a feedback control law together with a reduced order observer, which locally stabilizes a two dimensional thermal fluid modeled by the Boussinesq approximation. The authors proposed to use a linear Luenberger observer based on point observations of the linearized Boussinesq equations. However, no uncertainties were considered in the observer design and its performance evaluation.

The problem of designing a robust observer for the Boussinesq equations has been studied in [12], where the authors first used POD for model reduction, followed by a Luenberger-like observer design, based on the notion of input-state stability with respect to parameter uncertainties. These uncertainties were then estimated online using a data-driven optimization algorithm.

3

In this paper, we propose a robust observer for the 2D Boussinesq equations with parametric uncertainties, based on a methodology that we introduced in [1] for a class of spectral infinite-dimensional nonlinear systems. The observer is designed to be robust to bounded additive uncertainties, and includes a data-driven gain auto-tuning feature.

We want to underline here that the proposed approach is based on reduced order modeling of the Boussinesq equation, more specifically for a lock-exchange flow problem in 2D. There have been many studies of reduced order modeling for the lock-exchange flow problem, e.g., [23–26], however, in this line of work the goal of the reduced order model (ROM) is different from our goal in this paper. Indeed, in the existing ROM literature the goal is to approximate the original PDE model with a reduced order model which leads, for a given initial condition and given experimental conditions, to open-loop solutions that are close to the original PDE open-loop solutions for the same conditions. In contrast, in this work we seek to design a mathematical dynamical model, a.k.a. observer, which is based on a ROM of the original PDE, however, this ROM-based observer admits solutions that are convergent to the true solutions of the original PDE model, for different initial conditions and possibly different experimental conditions, e.g., a mismatch in the Reynolds number. This is due to the fact that we include in the observer design terms that are based on sparse real-time measurements from the observed system, i.e., from the solutions of the original PDE. These measurements, together with the proper design of the observer dynamics based on robust control theory, allows for the correction of both initial condition mismatches and model uncertainties, as we will see in the remaining of the paper.

In the sequel, we begin by introducing some basic definitions and notation in Section 2. Section 3 recalls, for completeness, the observer design briefly without restating the proofs that can be found in [1]. This approach is then applied to the challenging uncertain 2D Boussinesq equations in Section 4, which constitutes the main contribution of this paper. Concluding remarks are given in Section 5.

2   Basic Notation and Definitions

For a vector $q \in \mathbb{R}^n$, the transpose is denoted by $q^\top$. The Euclidean vector norm for $q \in \mathbb{R}^n$ is denoted by $\| \cdot \|$ so that $\|q\| = \sqrt{q^\top q}$. The Frobenius norm of a matrix $A \in \mathbb{R}^{n \times m}$, with elements a_{ij}, is defined as $\|A\|_F \triangleq \sqrt{\sum_{i=1}^{1=n} \sum_{j=1}^{j=m} |a_{ij}|^2}$. The Kronecker delta function is defined as: $\delta_{ij} = 0$, for $i \neq j$ and $\delta_{ii} = 1$. For a symmetric matrix $D \in \mathbb{R}^{n \times n}$, $\lambda_{\max}(D)$ denotes its maximum eigenvalue. We shall abbreviate the time derivative by $\dot{f}(t,x) = \frac{\partial}{\partial t} f(t,x)$, and consider the following Hilbert space: $\mathcal{H} = L^2(\Omega)$, $\mathcal{Z}_1 = H^1_{\mathrm{div}}(\Omega) \subset (\mathcal{H})^d, d = 2$ for velocity and $\mathcal{Z}_2 = H^1(\Omega) \subset \mathcal{H}$ for temperature. Thus, $\mathcal{Z}_1$ is the space of divergence-free vector fields on Ω with components in $H^1(\Omega)$. Fixed Dirichlet boundary conditions are also specified in the definition of the sets $\mathcal{Z}_1$ and $\mathcal{Z}_2$. We define the inner product $\langle \cdot, \cdot \rangle_{\mathcal{H}}$ and the associated norm $\| \cdot \|_{\mathcal{H}}$ on $\mathcal{H}$ as $\langle f, g \rangle_{\mathcal{H}} = \int_\Omega f(x)g(x)dx$, for $f, g \in \mathcal{H}$, and $\|f\|_{\mathcal{H}}^2 = \int_\Omega |f(x)|^2 dx$. A function $T(t,x)$ is in $L^2([0, t_f]; \mathcal{H})$ if for each $0 \leq t \leq t_f$, $T(t, \cdot) \in \mathcal{H}$, and $\int_0^{t_f} \|T(t, \cdot)\|_{\mathcal{H}}^2 dt < \infty$ with analogous definitions for the vector valued functions in $(\mathcal{H})^d, d = 2$. To generalize the discussion below, we consider the abstract Hilbert space $\mathcal{Z}$, and later specialize to $\mathcal{Z} = \mathcal{Z}_1 \times \mathcal{Z}_2$ when considering our Boussinesq equation examples.

3   Review of Observer Design

We consider the state estimation problem for nonlinear systems of the form

$$
\begin{aligned}
\dot{z}(t) &= Az(t) + Bu(t) + h(z(t), u(t)), \quad z(0) = z_0, \\
y(t) &= Cz(t),
\end{aligned}
\tag{1}
$$

where $z_0 \in D(A) \subset \mathcal{H}$, A is a linear operator that generates a C_0-semigroup on the Hilbert space $\mathcal{H}$, $B : \mathbb{R}^m \to \mathcal{H}$ is an input operator, $C : D(A) \to \mathbb{R}^p$ is the bounded linear operator for measurements, and h contains higher-order terms. For the well-posedness of the estimation problem, we assume that system (1) satisfies the following assumptions.

Assumption 1 *The Cauchy problem for equation (1) has a solution with bounded norm $\|z(t)\|_{\mathcal{H}}$ for any initial condition $z_0 \in D(A)$, and any $t > 0$.*

Assumption 2 *The function $h : D(A) \times \mathbb{R}^m \to [D(A)]'$ satisfies $h(0,0) = 0$ and the local Lipschitz plus constant assumption: there is a nonnegative constant β and for every pair $(z, u) \in D(A) \times \mathbb{R}^m$, there exist positive constants ϵ_z, ϵ_u, L_z, and L_u such that*

$$\|h(z,u) - h(\tilde{z}, \tilde{u})\|_{\mathcal{H}} \leq L_z \|z - \tilde{z}\|_{\mathcal{H}} + L_u \|u - \tilde{u}\|_{\mathbb{R}^m} + \beta,$$

for all $(\tilde{z}, \tilde{u}) \in D(A) \times \mathbb{R}^m$ satisfying

$$\|z - \tilde{z}\|_{\mathcal{H}} < \epsilon_z \qquad and \qquad \|u - \tilde{u}\|_{\mathbb{R}^m} < \epsilon_u.$$

Consider an observer with the following structure

$$\dot{\hat{z}}(t) = A_c \hat{z}(t) + B_c u(t) + F y(t) + G(\hat{z}(t), u(t)), \tag{2}$$

with $\hat{z}(0) = \hat{z}_0 \in D(A_c)$, and where $A_c : \hat{\mathcal{H}} \to \hat{\mathcal{H}}$, $B_c : \mathbb{R}^m \to \hat{\mathcal{H}}$, $F : \mathbb{R}^p \to \hat{\mathcal{H}}$, and $G : \hat{\mathcal{H}} \times \mathbb{R}^m \to \hat{\mathcal{H}}$ are to be determined, where $\hat{\mathcal{H}} \subset \mathcal{H}$ is a low-dimensional subspace that inherits the norm of $\mathcal{H}$, i.e., $\|\cdot\|_{\hat{\mathcal{H}}} = \|\cdot\|_{\mathcal{H}}$.

Possible choices for $\hat{\mathcal{H}}$ may be the space spanned by a set of dominant eigenfunctions of A (a modal approximation) or a set of basis functions obtained by performing a proper orthogonal decomposition (POD) of a collection of simulations of (1) and truncating (a POD approximation), e.g. [13,14]. Other basis function choices might be required for different PDEs, as explained in Remark 2 in Appendix.

Let $\mathcal{T} : \mathcal{H} \to \hat{\mathcal{H}}$ be the orthogonal projector from $\mathcal{H}$ to $\hat{\mathcal{H}}$ (hence, $\|\mathcal{T}\|_{\mathcal{H}} = 1$) and $\mathcal{T}^\dagger$ be the injection from $\hat{\mathcal{H}}$ into $\mathcal{H}$: $\mathcal{T}^\dagger \hat{z} = z$ for all $\hat{z} \in \hat{\mathcal{H}} \subset \mathcal{H}$. Then we define the *reduced estimation error* as

$$e(t) = \hat{z}(t) - \mathcal{T} z(t) \in \hat{\mathcal{H}}. \tag{3}$$

This can be used as a proxy for the *state estimation error*

$$e_{\text{se}} \equiv \mathcal{T}^\dagger \hat{z} - z \in \mathcal{H}, \tag{4}$$

6

when $\mathcal{T}$ produces a small projection error $(z - \mathcal{T}^\dagger \mathcal{T} z)$, since

$$e_{\text{se}}(t) = \mathcal{T}^\dagger e(t) - \left(z(t) - \mathcal{T}^\dagger \mathcal{T} z(t)\right). \tag{5}$$

When $\hat{\mathcal{H}}$ is the span of r dominant POD basis functions and $\mathcal{T}_{\text{POD}}$ is the corresponding projection for a specific trajectory z, then $\mathcal{T}_{\text{POD}}$ minimizes the projection error

$$\mathcal{P}(\mathcal{T}, z) = \left(\int_0^{t_f} \|z(t) - \mathcal{T}^\dagger \mathcal{T} z(t)\|_{\mathcal{H}}^2 \, dt\right)^{1/2}, \tag{6}$$

over all projections $\mathcal{T}$ into subspaces of $\mathcal{H}$ with dimension r, and where t_f denotes the finite time support over which the projection error is evaluated, cf. [13].

We then choose

$$B_c = \mathcal{T}B \qquad \text{and} \qquad G(\hat{z}, u) = \mathcal{T}h(\mathcal{T}^\dagger \hat{z}, u) \tag{7}$$

for all $\hat{z} \in \hat{\mathcal{H}}$ and $u \in \mathbb{R}^m$.

We have shown in [1] that the solutions of the state observer defined by (2) and (7) converges to the solutions of the states of the system (1) under Assumptions 1, 2, if F, A_c, and $\mathcal{T}$ satisfy the conditions

$$\left[A_c \mathcal{T} - \mathcal{T}A + FC\right] z = 0, \qquad \text{for all } z \in D(A), \tag{8}$$

$$\|\exp(A_c t)\|_{\hat{\mathcal{H}}} \leq M \exp(-\delta t), \qquad \text{for all } t > 0 \tag{9}$$

and,

$$\delta > ML_z, \tag{10}$$

where $M \geq 1$ and $\delta > 0$.

As mentioned above, one possible choice for the design of the projection operator $\mathcal{T}$ is the use of a POD approximation.

POD-based models are most known for retaining a maximal amount of energy in the reduced-order model [13, 14]. A POD basis is computed from a collection of s time snapshots This approximation could be obtained using a numerical method, such as FEM, or using direct measurements of the system modeled by the PDE, if feasible. In this paper, the POD basis is computed

from snapshots of approximate numerical solutions of the partial differential equation.

To this end, we compute a set of s snapshots of approximate solutions as

$$\mathcal{S} = \{z_n(t_1, \cdot), ..., z_n(t_s, \cdot)\} \subset \mathcal{Z}^n \subset \mathcal{H}, \tag{11}$$

of the dynamical system, usually obtained from a discretized approximation of the model (1) in n dimensions. The $\{t_i\}_{i=1}^s$ are time instances at which snapshots are recorded, and do not have to be uniformly spaced in general, though for simplification, we assume uniformly spaced samples below. The *correlation matrix* K is then defined as

$$K_{ij} = \frac{1}{s} \langle z_n(t_i, \cdot), z_n(t_j, \cdot) \rangle_{\mathcal{H}}, \ i, j = 1, ..., s. \tag{12}$$

The normalized eigenvalues and eigenvectors of K are denoted by λ_i and v_i, respectively. Note that the λ_i are also referred to as the *POD eigenvalues*.

The ith *POD basis function* is computed as

$$\phi_i(x) = \frac{1}{\sqrt{s}\sqrt{\lambda_i}} \sum_{j=1}^s [v_i]_j z_n(t_j, x), \ i = 1, ..., r, \tag{13}$$

where $r \leq \min\{s, n\}$ is the number of retained POD basis functions and depends upon the application. The POD basis functions are orthonormal:

$$\langle \phi_i, \phi_j \rangle_{\mathcal{H}} = \int_{\Omega} \phi_i(x)^* \phi_j(x) dx = \delta_{ij}, \tag{14}$$

where δ_{ij} denotes the Kronecker delta function. In practice, it is more numerically stable to compute the POD bases using a generalized singular value decomposition (SVD) of the snapshot data $\mathcal{S}$. This is related to the SVD, except that it ensures that the orthogonality condition (14) holds.

Indeed, in this case we can approximate solutions to (1) in $\hat{\mathcal{H}}_r$ using

$$z_r^{pod}(t, \cdot) = \sum_{i=1}^r q_i(t) \phi_i(\cdot) \ \in \hat{\mathcal{H}}_r, \tag{15}$$

where $q_i, \ i = 1, ..., r$ are the POD projection coefficients, and $\phi_i, \ i = 1, ..., r$ are the POD basis functions. Note that $q_i(t) = \int_{\Omega} \phi_i(x)^* z_n(t, x) dx$.

We then define the (orthogonal) projection operator $\mathcal{T} \equiv \mathcal{T}_{\mathrm{POD}} : \mathcal{H} \to \hat{\mathcal{H}}_r$ as follows

$$[\mathcal{T}_{\mathrm{POD}}z]\,(\cdot) = \sum_{i=1}^{r} \phi_i(\cdot)\langle \phi_i, z \rangle_{\mathcal{H}}. \tag{16}$$

The pseudo-inverse of $\mathcal{T}$ is the injection of $\hat{\mathcal{H}}_r$ into $\mathcal{H}$. Thus $\mathcal{T}^\dagger \hat{z} = z$ for all $\hat{z} \in \hat{\mathcal{H}}_r$ and since $\mathcal{T}$ is a projection operator, we have $\mathcal{T}\mathcal{T}^\dagger = \mathcal{I}_r$.

Next, we define $A_c : \hat{\mathcal{H}}_r \to \hat{\mathcal{H}}_r$ as

$$A_c = \mathcal{T}^{\dagger^*} A \mathcal{T}^\dagger. \tag{17}$$

With this selection, we can show that for any $\hat{z} \in \hat{\mathcal{H}}_r$ with $\|\hat{z}\|_{\hat{\mathcal{H}}} = 1$, the following holds: $\langle A_c \hat{z}, \hat{z} \rangle = \langle A\mathcal{T}^\dagger \hat{z}, \mathcal{T}^\dagger \hat{z} \rangle \le \max_{\|z\|_{\mathcal{H}}=1} \langle Az, z \rangle$.

Finally, to satisfy condition (8), we define F as

$$F = (\mathcal{T}A - A_c\mathcal{T})C^\dagger, \tag{18}$$

where $C^\dagger$ is a left pseudo-inverse of the bounded linear operator C, and $C^\dagger C$ is a projection onto the complement of the null space of C.

3.1 Robust Observer Design

Let us consider the case where the system (1) contains an uncertainty on h, as follows

$$\dot{z}(t) = Az(t) + Bu(t) + h(z(t), u(t)) + \Delta h(z(t)), \tag{19a}$$

$$y(t) = Cz(t), \tag{19b}$$

from $z(0) = z_0$, where the uncertainty $\Delta h : \mathcal{H} \to \mathcal{H}$, satisfies the following assumption.

Assumption 3 *The uncertainty $\Delta h : \mathcal{H} \to \mathcal{H}$, is uniformly bounded: there exists a constant $\Delta h_{\max} > 0$ such that $\|\Delta h(z)\|_{\mathcal{H}} \le \Delta h_{\max}$, $\forall z \in \mathcal{H}$.*

Now, if we examine the dynamics of the observer (2), we see that the observer convergence relies on the design of the nonlinear function G, in (7). To robustify

the nominal design presented in Section 3, and account for the additional uncertainty term Δh, we use a Lyapunov redesign approach and add an additional term to G. The robust observer, where we use $\hat{z}$ to denote the estimate of z, is now written as

$$\dot{\hat{z}}(t) = A_c\hat{z}(t) + B_cu(t) + Fy(t) + G(\hat{z}, u) + \Delta G(\hat{z}), \tag{20}$$

with A_c, B_c, F, G satisfying conditions (7), (8), (9),(10), and where $\Delta G : \hat{\mathcal{H}} \to \hat{\mathcal{H}}$, must be designed to compensate for any negative impact that the uncertainty Δh might have on the convergence of e.

Carrying out a similar analysis for the robust observer (20), under (7), and (8), the associated error dynamics satisfy

$$\begin{aligned}\dot{e}(t) =& A_ce(t) + G\left(e(t) + Tz(t), u(t)\right) \\ &- \mathcal{T}h(z(t), u(t)) + \Delta G(\hat{z}) - \mathcal{T}\Delta h(z),\end{aligned} \tag{21}$$

where, ΔG is defined as

$$\Delta G(\hat{z}) = k\Delta h_{\max}\tilde{C}^*\tilde{C}e, \tag{22}$$

for $k < 0$, and $\tilde{C}$ satisfying

$$\tilde{C}\mathcal{T} = C. \tag{23}$$

It is shown in [1] that the solutions of the error dynamics (21) for the observer (7) and (20) , under Assumption 1, and conditions (8), (9), and (10), converge to the invariant set

$$S = \{e \in \hat{\mathcal{H}}, \text{ satisfying, } k\|e\|_{\hat{\mathcal{H}}}\lambda_{\min}(\tilde{C}^*\tilde{C}) + 1 \geq 0\},$$

and the estimation error upper-bound is given by

$$\|e(t)\|_{\hat{\mathcal{H}}} \leq \frac{-1}{k\lambda_{\min}(\tilde{C}^*\tilde{C})} + (\|e(0)\|_{\hat{\mathcal{H}}} + \frac{1}{k\lambda_{\min}(\tilde{C}^*\tilde{C})})\exp(k\Delta h_{\max}\lambda_{\min}(\tilde{C}^*\tilde{C})t). \tag{24}$$

3.2   Learning-based Tuning of the Observer

In this section we want to merge together the passive robust observer given by (20), and (22), with an active learning algorithm, to improve the performance

of the observer.

To find the optimal value of the observer gain, we propose to use a data-driven optimization algorithm to auto-tune the gain online, while the observer is estimating the system states. This problem is strongly related to iterative feedback tuning (IFT), e.g., [17–21]. We will follow [20,21], and use an extremum seeking (ES)-based auto-tuning approach.

We first write the feedback gain as

$$k = k_{\mathrm{nom}} + \delta k, \; k_{\mathrm{nom}} < 0, \tag{25}$$

where k_{nom} represents the nominal value of the observer gain, and δk is the necessary adjustment of the gain to improve the transient performance of the observer.

We then define the learning cost function

$$\begin{aligned} Q(\delta k) &= \int_0^T ||e_y||_{\mathcal{H}}^2 dt, \\ e_y(\delta k) &= \hat{y}(t; \delta k) - y(t), \\ \hat{y} &= C\hat{z}, \end{aligned} \tag{26}$$

where $T > 0$, $\hat{z}$ is solution of the observer (20), (22), and y is the measured output. Furthermore, for analysis purposes, we will need the following assumptions on Q.

Assumption 4 *The cost function $Q(\delta k)$ in (26) has a local minimum at $\delta k = \delta k_*$.*

In order to tune δk we propose to use the time-varying amplitude-based ES algorithm, e.g., [22],

$$\begin{aligned} \dot{x}_k &= -\delta_k \omega_k \sin(\omega_k t) Q(\delta k), \\ \delta k(t) &= x_k(t) + a_k \sin(\omega_k t), \\ \dot{a}_k &= -\delta_k \omega_k \epsilon_k a_k, \end{aligned} \tag{27}$$

where $\delta_k > 0$, $\omega_k > 0$, $\epsilon_k > 0$.

11

More explicitly the gain k is tuned by the following updates:

$$k(t) = k_{\text{nom}} + \Delta k(t), \quad k_{\text{nom}} < 0$$
$$\Delta k(t) = \delta k((j-1)\Delta t), \ (j-1)\Delta t \le t < j\Delta t, \ j = 1, 2, 3... \tag{28}$$

where δk is defined by the forward first order Euler discretization of (26), (27), with a time step equal to Δt.

It is shown in [1] that the observer (7), (20), and (22), where the gain k is tuned iteratively using (26), (27), and (28) leads to uniformly bounded state estimates, and that under Assumption 4, the gain k converges to a neighborhood of its local optimum value $k_{\text{nom}} + \delta k_*$.

4   Main Result: Observer design for the Uncertain Boussinesq equations

4.1   Formulating the Boussinesq estimation problem under model uncertainties

We consider the (uncertain) incompressible Boussinesq equations that describe the evolution of velocity $\mathbf{v}$, pressure p, and temperature T of a fluid. This system could serve as a model for the flow of air and temperature in a room. The coupled equations reflect the conservation of momentum, mass, and energy, respectively

$$\frac{\partial \mathbf{v}}{\partial t} + \mathbf{v} \cdot \nabla \mathbf{v} = -\nabla p + \nabla \cdot \tau(\mathbf{v}) + \text{Ri} T\, \widehat{\mathbf{e}}_3, \tag{29}$$

$$\nabla \cdot \mathbf{v} = 0, \tag{30}$$

$$\frac{\partial T}{\partial t} + \mathbf{v} \cdot \nabla T = \nabla \cdot \left(\frac{1}{\tilde{\text{Re}}\text{Pr}} \nabla T \right), \tag{31}$$

where $\tilde{\text{Re}}$ is the uncertain Reynolds number, s.t., $\tilde{\text{Re}} = \text{Re}_{\text{nom}} + \Delta \text{R}_{\text{e}}$, Re_{nom} is the nominal known value of the Reynolds number, and ΔR_e models the unknown change in the Reynolds number. This might be due to a temperature or humidity change that affects some of the material properties used in the

nondimensionalization, such as the density and viscosity, or a rescaling of the nominal velocity in the system. Pr is the Prandtl number, Ri is the Richardson number, and $\tau(\mathbf{v}) = \frac{1}{\mathrm{Re}}(\nabla\mathbf{v} + \nabla\mathbf{v}^\top)$ cf. [23]. We write (29)-(31) in the state-space form

$$
\begin{aligned}
\dot{z}(t) &= Az(t) + Bu(t) + h(z(t), u(t)) + \Delta h(z(t)), \quad z(0) = z_0, \\
y(t) &= Cz(t),
\end{aligned}
\tag{32}
$$

where, $z = (v, T)^\top \in \mathcal{Z}_1 \times \mathcal{Z}_2$, the A operator, written to emphasize the upper triangular structure, is defined as

$$
Az = \left[
\begin{array}{ccc}
\frac{1}{\mathrm{Re}}\nabla\cdot(\nabla\mathbf{v} + \nabla\mathbf{v}^\top) & + & \mathrm{Ri}\, T\boldsymbol{e}_3 \\
0 & + & \frac{1}{\mathrm{RePr}}\Delta T
\end{array}
\right],
\tag{33}
$$

while the nonlinear term is

$$
h(z, u) = (-\mathbf{v}\cdot\nabla\mathbf{v}, -\mathbf{v}\cdot\nabla\mathbf{T})^\top,
\tag{34}
$$

$$
\Delta h = \left[
\begin{array}{c}
\Delta\mu\nabla\cdot(\nabla\mathbf{v} + \nabla\mathbf{v}^\top) \\
\Delta\mu\frac{1}{\mathrm{Pr}}\Delta T
\end{array}
\right],
\tag{35}
$$

$$
\Delta\mu = \frac{-\Delta Re}{Re_{\mathrm{nom}}(Re_{\mathrm{nom}} + \Delta R_e)}
$$

$B = 0$, and $C : D(A) \to \mathbb{R}^p$ is the bounded linear operator for measurements, defined as

$$
y(t) = \left(\int_{\Omega_1} z(t, x)dx, ..., \int_{\Omega_p} z(t, x)dx\right)^\top =: Cz(t).
\tag{36}
$$

We assume that the sensors record the average temperature and velocity over selected subdomains Ω_i, $i = 1, ..., p$.

4.2   Numerical solver and test-case setup

Our numerical example consists of the lock-exchange problem where a fluid in an elongated domain is initially at rest but has two distinct air temperatures (or salinity for water) on either side of a gate. The gate is removed at $t = 0$ and buoyancy forces created by the change in temperature drives the evolution of the fluid flow. Note that this test problem has been used to study POD-based reduced-order models in a number of recent papers, see for example [24–26].

The Boussinesq equations are solved in the domain $\Omega = (0,8) \times (0,1)$ and over the time interval $[0, 16]$ ($t_f = 16$) using a mixed formulation with the Taylor-Hood finite element pair for the velocity and pressure coupled with a quadratic finite element approximation for the temperature. We proceed with two sets of numerical tests, corresponding to two different flows, one laminar characterized by a low Reynolds number Re = 88 which is usually associated with weak multi-scale interactions and considered to be numerically easier to solve, and one more dominant nonlinear effects ("turbulent")[2] characterized by a higher Reynolds number Re = 8,800. In the laminar case we use a coarse mesh with 513×65 equally spaced nodes and connected to form $16,384$ quadratic finite elements. In the second case, a fine mesh with $2,049 \times 257$ equally spaced nodes and connected to form $262,144$ quadratic finite elements were used. A novelty of these meshes is that the elements are symmetrically arranged (i.e. preserving x- and y-reflections as well as rotational symmetries about the center point $(4, 0.5)$). These finite elements were used for the spatial discretization of functions in Ω. The time discretization is performed using a Crank-Nicolson method with $\Delta t = 2 \times 10^{-3}$ for the Re = 88 and $\Delta t = 2.5 \times 10^{-4}$ for the Re = 8,800 simulations. A penalty method was used to impose the incompressibility constraint. See [27] for more details. Our example uses $\mathbf{v}(0, \cdot) = \mathbf{0}$ and sets the initial temperature for the lock-exchange problem to be $T(0, \cdot)$ to be -0.5 for $x \in (0, 4)$, 0.5 for $x \in (4, 8)$ and 0 otherwise. No-slip boundary conditions for $\mathbf{v}$ and insulated boundary conditions for T are used over the entire boundary of Ω. The symmetries and anti-symmetries of the solutions are imposed throughout the numerical simulation. For the simulations used to generate our data in the case of laminar flow, we used the parameters Re = 88, Pr = 0.712, and Ri = 12.9132. In the case of high Reynolds number flow, we used the parameters Re = 8800, with the same values of Pr and Ri. These non-dimensional parameters are based on the height of the domain (4.08 m), and the initial temperature difference $1°K$,

---

[2]We do not mean that this turbulent flow corresponds to any physical flow, since the tests are done in 2D, but we mean that the case is challenging to solve numerically due to the strong multiscale interactions associated with high Reynolds numbers.

a nominal velocity of (0.0325m/s), $\beta = 3.43 \times 10^{-3}/°K$, and the parameters for air at 293°K ($\rho = 1.205 kg/m^3$, $\nu = 1.511 \times 10^{-5}$, $c_p = 1005 J/kg°K$, and $\kappa = 0.0257 kg \ m/°Ks$). The simulation data for the case Re = 88 was used to compute ten temperature POD modes and ten velocity POD modes. For the more challenging case Re = 8800 the data was used to compute twenty temperature POD modes and twenty velocity POD modes. These POD basis are then used to build our $\mathcal{T}_{\text{POD}}$ operators (16) in our observer design as discussed in the section below. We also underline here that the cases with high Reynolds numbers in 2D used here are not meant to represent any physical configuration, since physical turbulent flows cannot be represented by 2D Boussinesq equations.

4.3   Comments on the observer design

In this section, we provide commentary on applicability of the theoretical justification for our observer design for the Boussineq equations.

First, note that the operator A, defined in (33), with $\mathcal{Z}_1 = \{\mathbf{v} \in \mathbf{H}^1 | \nabla \cdot \mathbf{v} = 0 \text{ in } \Omega, \mathbf{v} \cdot \mathbf{n} = 0 \text{ on } \partial\Omega\}$ and $\mathcal{Z}_2 = L_2(\Omega)$ generates a C_0-semigroup cf. [28].

Second, although we know that Assumption 2 does not hold in the case of the challenging Boussinesq equations[3], we observe[4] in Figure 1 that the maximum of the $\|.\|_{\mathcal{H}}$-norm of the gradient of h over space and time is indeed bounded in our case along the test trajectories, thus the computed solutions that we are considering in these tests observe a local Lipschitz-like bound along the computed trajectories. If this held in general, the Lipschitz constant could be equated to the maximum of the gradient norm.

To compute the matrices for the nominal observer (2) and (7), we computed the POD projection matrix $\mathcal{T}_{POD}$ using[5] in the first laminar case 10 POD ba-

---

[3]Unfortunately, the existence and uniqueness of solutions for the Boussinesq equations is still an open problem, thus we cannot claim that Assumption 2 is valid in this case for all boundary and initial conditions, since we cannot guarantee the existence of a bounded smooth solution for all cases.

[4]Similar plots have been obtained for both Reynolds numbers.

[5]We underline here that this choice is empirical and cannot be determined beforehand in closed-from. However, one way to numerically determine the minimal number of PODs is to

sis functions for the velocity and 10 POD basis functions for the temperature variables computed from snapshots taken every $\Delta t = 2 \times 10^{-3}$, and in the second turbulent case 20 POD basis functions for the velocity and 20 POD basis functions for the temperature variables computed from snapshots taken every $\Delta t = 2 \times 10^{-3}$. The projection matrix has been computed using the 20 POD basis function in the first case, and the 40 POD basis functions in the second case. Then, the matrix A_c has been computed using equation (17), which led to a stable matrix with a maximum eigenvalue of -1.5 in the first case, and -10 in the second case.

We consider $p = 20$, and $p = 40$ measurements of the form (36), for the first and second case, respectively. These sensors record the average temperature and the velocity component averages were taken at ten unique locations for each quantity and selected using the Q-DEIM algorithm [29]. In particular, this algorithm was used to find those point locations that best distinguish the POD modes. The size of the integration intervals Ω_i, $i = 1, ..., p$ was selected as 0.03×0.03. Furthermore, to simulate a more realistic scenario, we added bounded measurement noise in the form of random additive disturbances of maximum value 10^{-3}.

Next, F has been computed as an approximation of the Sylvester equation in condition (8), using the solution given by equation (18). As explained in (Remark 1, in Appendix), due to the high discretization dimension needed to solve for the Boussinesq equation, e.g., in the second case the matrix C is in $\mathbb{R}^{40 \times 1579779}$, which makes solving for F challenging, i.e., the pseudo-inverse in (18) induces numerical errors, i.e., $\|A_c \mathcal{T} - \mathcal{T} A + FC\|_F = 0.0925$. In fact, we can see in Figure 2 the evolution of the norm of the residual term $\|Res_{D0} z\|_{\mathcal{H}}$ in time along the trajectories of our second case example[6]. We can see that this norm is bounded by a relatively large value equal to 12. However, this residual numerical error does not affect the convergence of the observer (see Remark 1, in

start with a large number of basis and gradually decrease the number until the estimation performance starts deteriorating, then pick the last number of PODs.

[6]Similar plots can be obtained for the first case.

Appendix). To verify numerically that condition (D1) is satisfied in the second test-case, we report in Figure 3, the Frobenius norm of $exp(A_c t)$, which shows a clear exponential decrease, with an estimate of $M = 6.325$, and an estimate of the decrease rate $\delta = 9.4932$, this leads to an upper-limit on L_z of about 1.5, for condition (D2) to be satisfied.
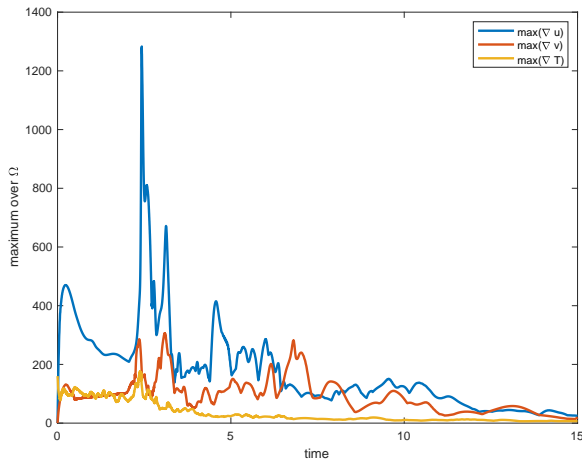
Figure 1: Maximum of $\|\nabla h\|_{\mathcal{H}}$ over Ω as function of the simulation time interval $[0, \ t_f]$

4.4 Numerical results- Nominal case (laminar flow)

We report in Figures 4, 5, and 6 the results of full-order finite element simulation of (29)-(31) for the first case, i.e., low Reynolds number Re = 88. The first snapshot, shown in Figure 4, is taken at the initial instant $t = 1$, the second snapshot, shown in Figure 5, corresponds to $t = 10$, and finally the third snap-
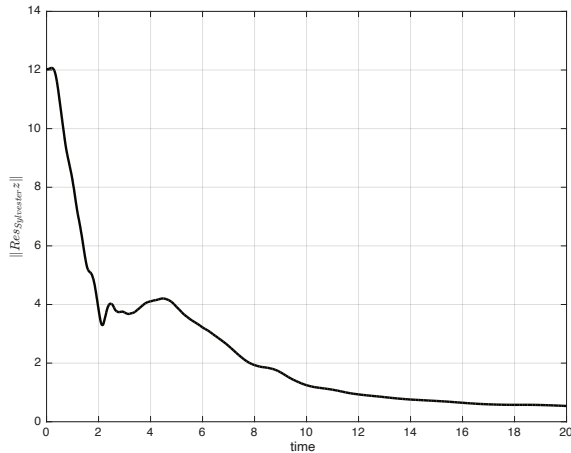
Figure 2: $\|Res_{D0}z\|_{\mathcal{H}}$ as function of nondimensional time

shot shown in Figure 6, corresponds to $t = 16$. We see in Figure 4 the setup of this experiment, where two fluids of different temperatures are separated by a vertical barrier at $x = 4$. On the right side of the barrier we have high temperature, whereas, on the left side of the barrier we have low temperature. Based on this setup, when we remove the barrier between the two fluids, we expect the low density, warmer fluid to rise, while the high density, cooler fluid sinks, as seen in Figure 4. In this case of low Reynolds number, we can observe that the flow is laminar with no vortices formation during transient, when these fluids slide past one another.

We test the observer (20), (22), with $k = -10^2$, and an artificial value for the uncertainty bound $\Delta h_{\max} = 1$. Note that we call $\Delta h_{\max}$ here to be artificial since we do not have any explicit model uncertainties, instead, this upper-bound is meant to take into account the additive errors obtained from

18
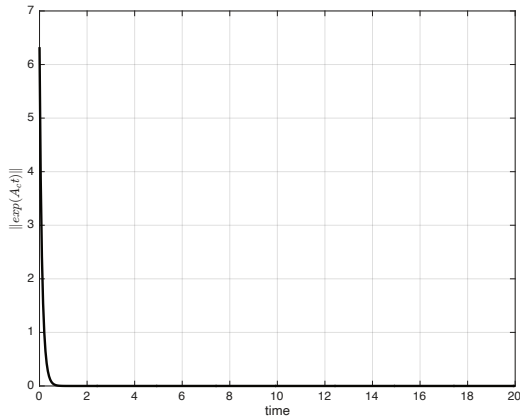
Figure 3: $\|exp(A_c t)\|_2$ as function of nondimensional time

the approximation (18), see (Remark 1, in Appendix). First we see in Figure 7 that the norm of the POD coefficient estimation error is decreasing fast, reaching a value less than 1 by $t = 2$. This is due to the direct influence of the feedback gain on the convergence rate, as shown in equation (24). This leads to a good estimation of the POD coefficients, as seen for example in Figure 8, where we report the first four POD coefficients for the velocity and temperature. We see that in this laminar case, there are no residual errors in the estimation. We will see later that this is not the case for the more challenging turbulent flow.

We report some snapshots obtained from the observer estimates. For instance, in Figure 9 we report the estimate of the velocity and temperature snapshots at $t = 1$, and the associated estimation error in Figure 10. We can see that the estimation error is large, which is due to the imposed initial errors on the estimated POD coefficients, see Figure 7. However, we can see in subse-

19

quent snapshots estimate, reported in Figure 11 for $t = 6$, Figure 13 for $t = 16$, that the observer quickly recovers a good estimation performance, as confirmed by the small estimation errors seen in Figure 12 for $t = 6$, and Figure 14 for $t = 16$.

Since this case of laminar flow was rather easy to estimate using a small feedback gain and since after testing several other gains we did not notice any major estimation performance difference, we will not test for this case the gain auto-tuning algorithm. We will test the robustness of the estimator, as well as, the gain auto-tuning on the more challenging turbulent flow case, as reported in the next section.

4.5   Numerical results- Nominal case (turbulent flow)

In Figures 15, 16, and 17 we present the full-order finite element simulation of (29)-(31). The first snapshot, shown in Figure 15, is taken at the initial instant $t = 1$, the second snapshot, shown in Figure 16, corresponds to $t = 10$, and finally the third snapshot shown in Figure 17, corresponds to $t = 14.4$. In this case of high Reynolds number, we can observe that vortices are generated, then diffuse as these fluids slide past one another.

First we report the results of the nominal observer, i.e., $k = 0$ in equations (20), (22). The $\|.\|_{\hat{\mathcal{H}}}$-norm of the estimation error e in equation (3), of the POD coefficients is shown in Figure 18. One can see that the norm of the error decreases as expected. However, the decrease rate is not optimal, since with this fluid example, most of the interesting dynamics of the fluid happens before $t = 4$, which means that the nominal observer, although stable, does not lead to a good estimation performance. This is due to the residual errors in approximately satisfying (8), as explained above, which implies a higher initial value of the error norm upper-bound [1], but also due to the slow error decay rate obtained from condition (10).

We saw in Section 3.1 that this performance can be improved by using the robustification term in the observer, i.e., $k \neq 0$. We now report the results

20
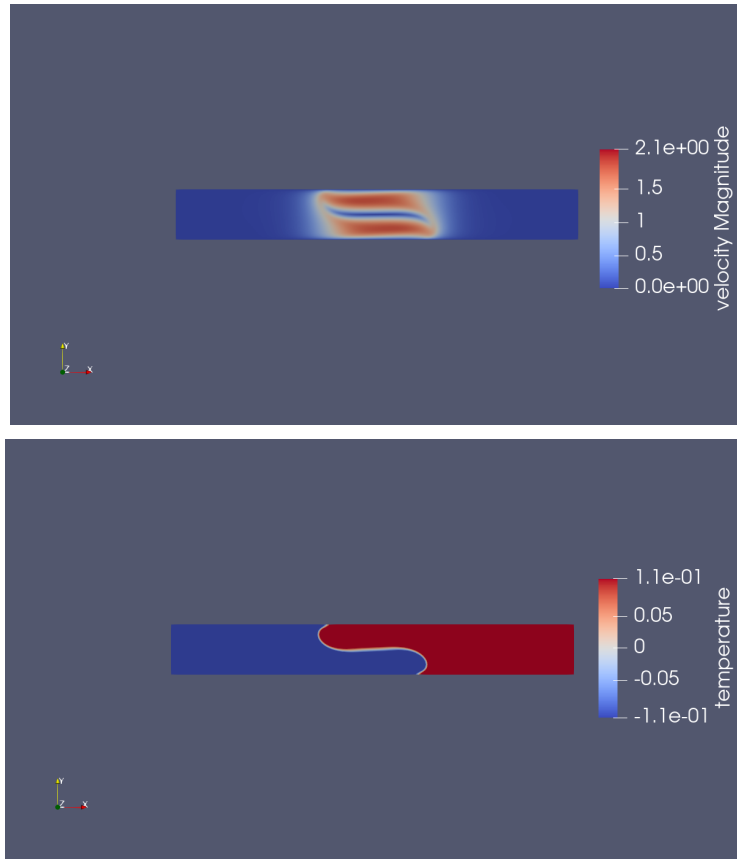
Figure 4: Case one: $\mathrm{Re} = 88$: True solution profile at $t = 1$ (Top: velocity, Bottom: temperature)
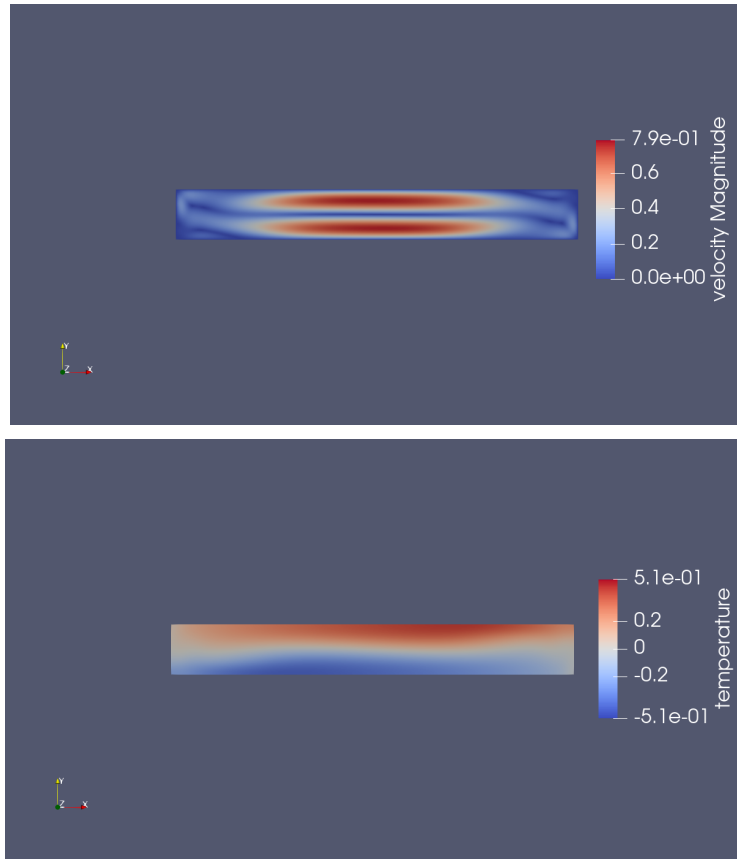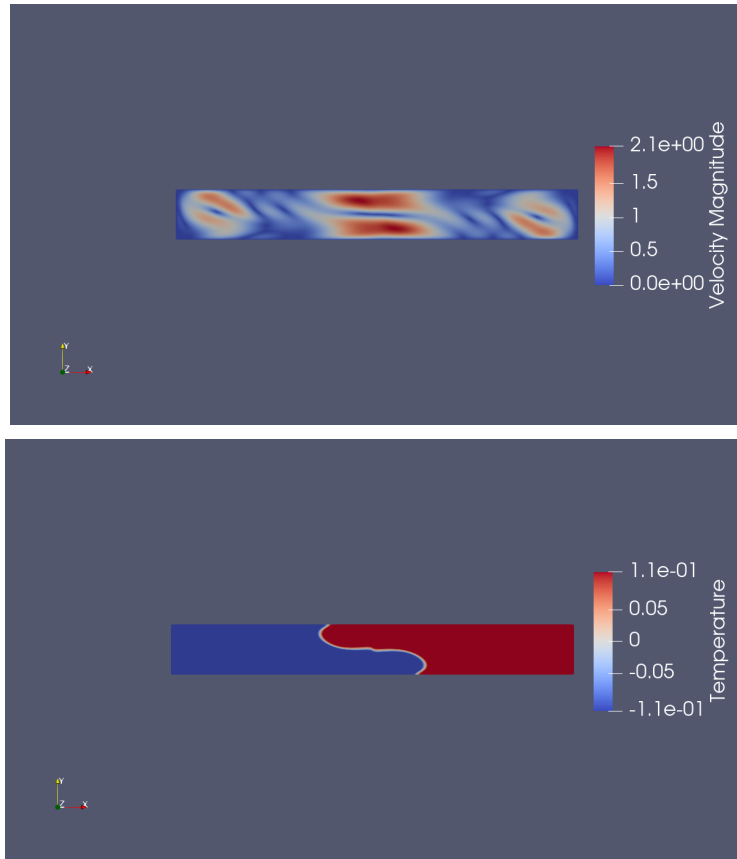
Figure 5: Case one: Re = 88: True solution profile at $t = 6$ (Top: velocity, Bottom: temperature)
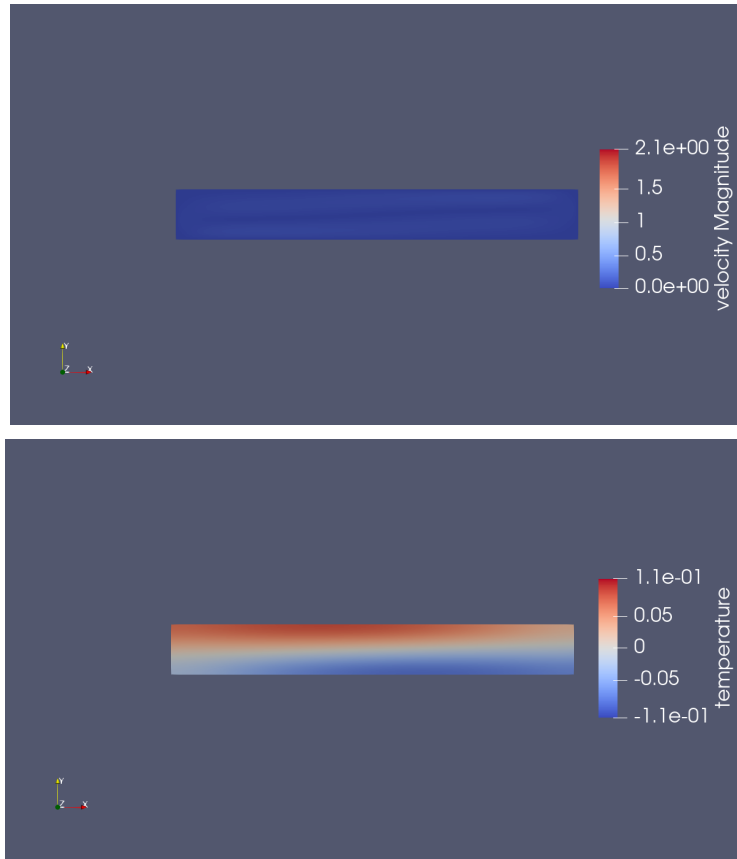
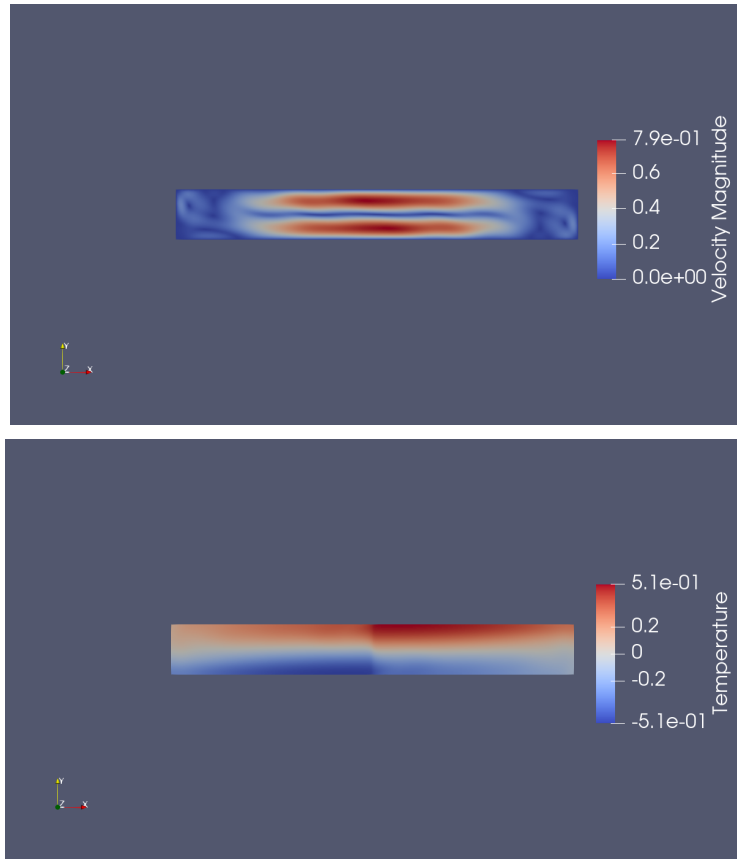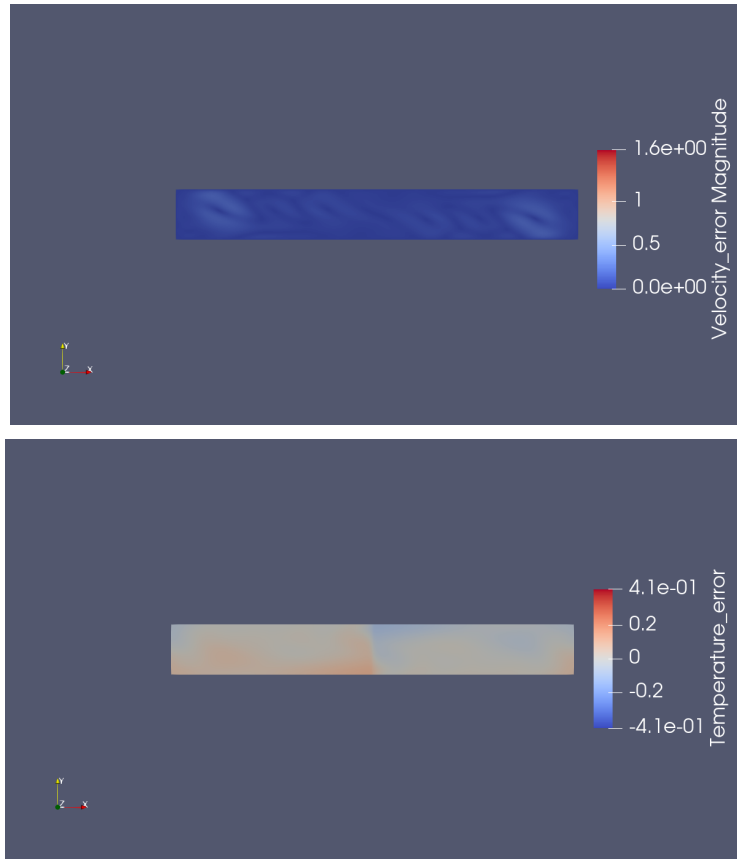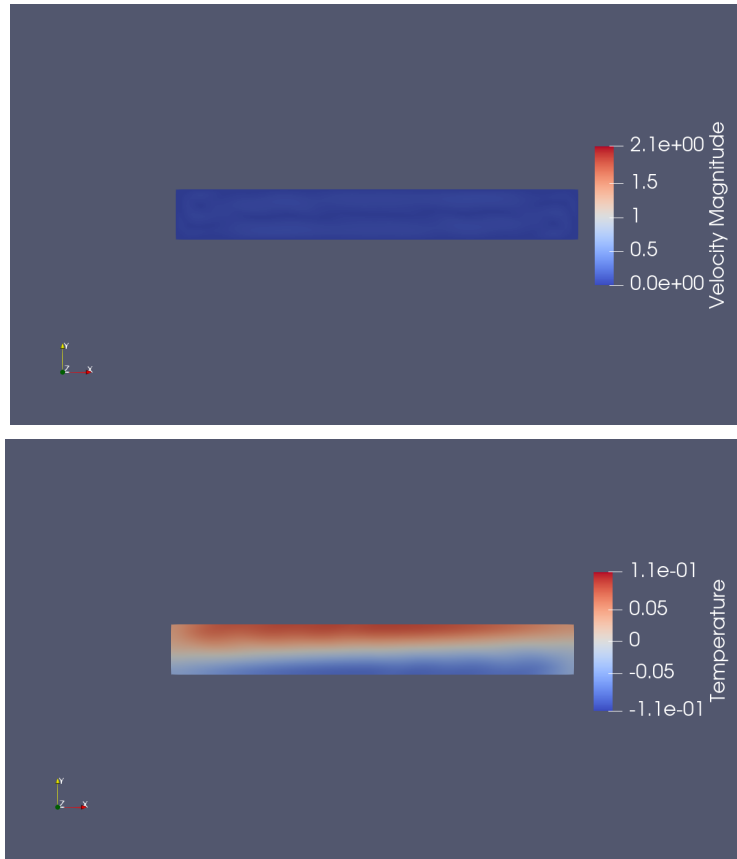Figure 6: Case one: $Re = 88$: True solution profile at $t = 16$ (Top: velocity, Bottom: temperature)
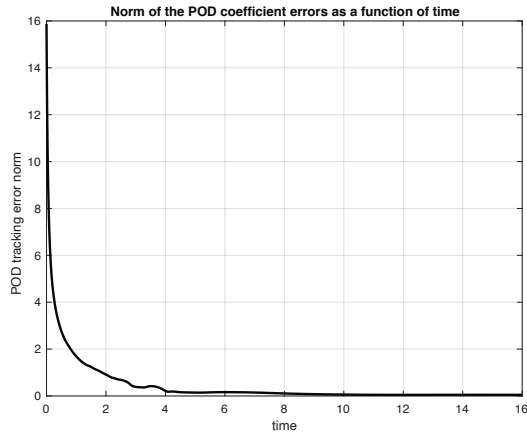
Figure 7: Case one: $\text{Re} = 88$: $\|e\|_{\hat{\mathcal{H}}}$ as function of time- nominal case with $k = -100$

corresponding to this case. We test the observer (20), (22), with $k = -10^5$, and an artificial value for the uncertainty bound $\Delta h_{\max} = 1$. Note that we call $\Delta h_{\max}$ here to be artificial since we do not have any explicit model uncertainties, instead, this upper-bound is meant to take into account the additive errors obtained from the approximation (18), see (Remark 1, in Appendix). First we see in Figure 19 that the norm of the POD coefficient estimation error is decreasing faster than in the case with no robustification shown in Figure 18. This is due to the direct influence of the feedback gain on the convergence rate, as shown in equation (24). This leads to a better estimation of the POD coefficients, as seen for example in Figure 20, where we report the first four POD coefficients for the velocity and temperature. We can see that some residual oscillations remain on the coefficients estimate, which are partly due to the fact

24
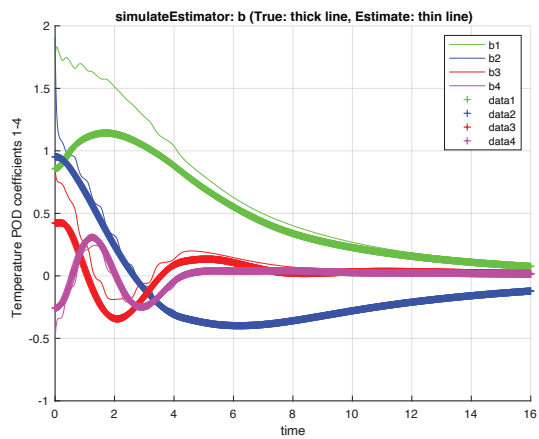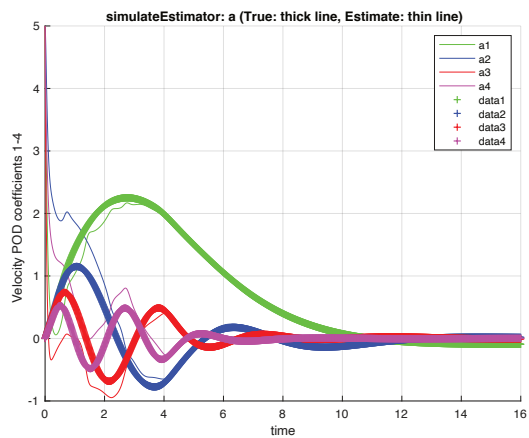
Figure 8: Case one: Re = 88: Estimated vs. actual POD coefficients over time, with $k = -100$ (Top: velocity PODs, Bottom: temperature PODs)

25

Figure 9: Case one: Re $= 88$: Estimated solution profile at $t = 1$, with $k = -100$ (Top: velocity, Bottom: temperature)
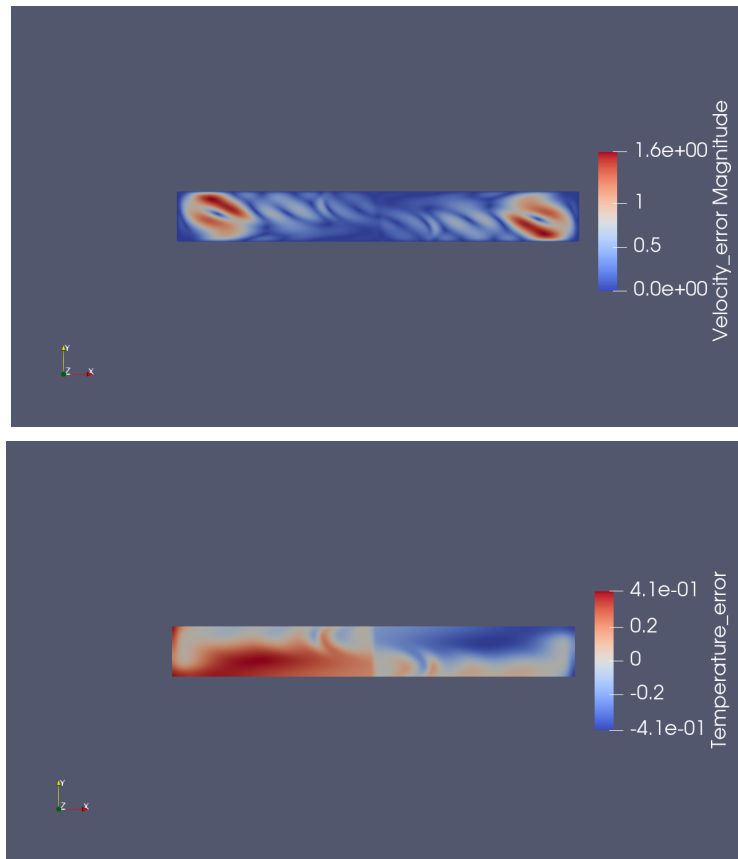
Figure 10: Case one: Re $= 88$: Estimated error profile at $t = 1$, with $k = -100$ (Top: velocity, Bottom: temperature)

Figure 11: Case one: Re = 88: Estimated profile at $t = 6$, with $k = -100$ (Top: velocity, Bottom: temperature)

Figure 12: Case one: Re = 88: Estimated error profile at $t = 6$, with $k = -100$ (Top: velocity, Bottom: temperature)

Figure 13: Case one: Re = 88: Estimated solution profile at $t = 16$, with $k = -100$ (Top: velocity, Bottom: temperature)
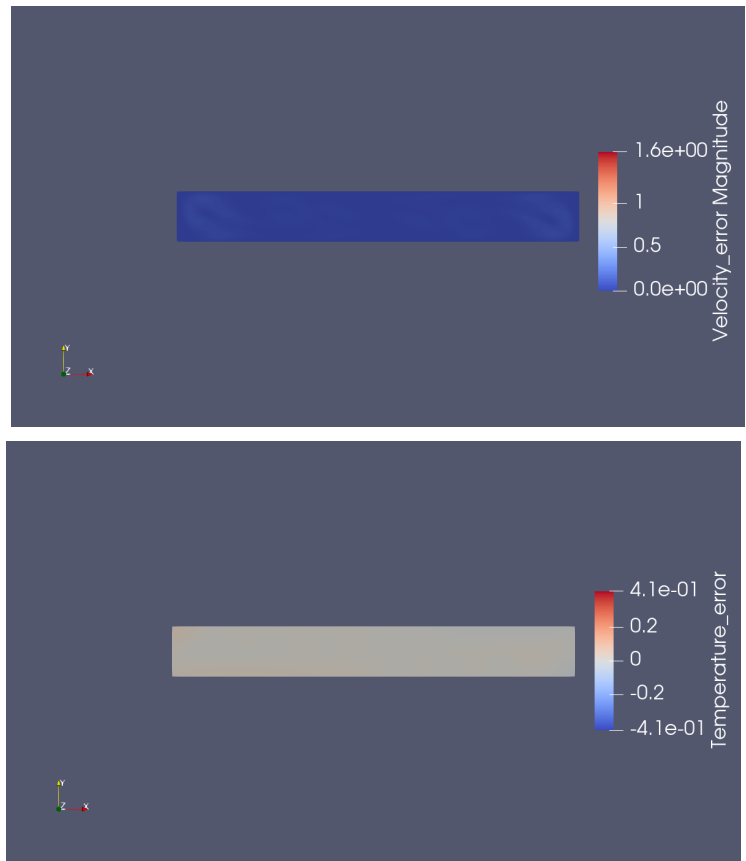
Figure 14: Case one: Re $= 88$: Estimated error profile at $t = 16$, with $k = -100$ (Top: velocity, Bottom: temperature)

that we are solely relying on noisy output measurements to reconstruct all the POD coefficients. These oscillations are also partly due to the truncation of higher POD modes, and we expect them to become more predominant if select a lower number of PODs to design the observer.

To better evaluate the estimation performance of the observer in this case, we also report some snapshots' estimates. For instance, in Figure 21 we report the estimate of the velocity and temperature snapshots at $t = 1$, and their associated estimation error in Figure 22. We can see that the estimation error is large, which is due to the imposed initial errors on the estimated POD coefficients, see Figure 19. However, we can see in subsequent snapshots' estimate, reported in Figures 23 for $t = 10$, Figure 25 for $t = 14.4$, that the observer quickly recovers a good estimation performance, as confirmed by the small estimation errors seen in Figures 24 for $t = 10$, and Figure 26 for $t = 14.4$.

4.6 Numerical results-Uncertain case

Let us consider now the case where there are explicit parametric uncertainties in the model. For instance, it is well known that in the setting of indoor airflow modeling, the Reynolds number Re in the Boussinesq model can change based on the room's airflow inlets size or based on the air conditioning system aging or degradation, e.g. [30]. In such cases, one can design the observer based on an initial nominal value of Re, however, the observer will be run based on measurements corresponding to a different flow, associated with a different actual Re. We choose to focus on uncertainties in the Reynolds number, since this case can clearly be cast in the form of our robust observer design presented in Section 3.1. Indeed, if we examine equations (33) and (34), we can see that an uncertainty in Re leads to an additive uncertainty term Δh as defined in (35).

To test this case, we use $\mathrm{Re} = 8800$ as the nominal value and $\mathrm{Re}_{actual} = 8000$ as the actual value of the Reynolds number, associated with the measurements that are fed back to the robust observer (20), (22). We implement the robust
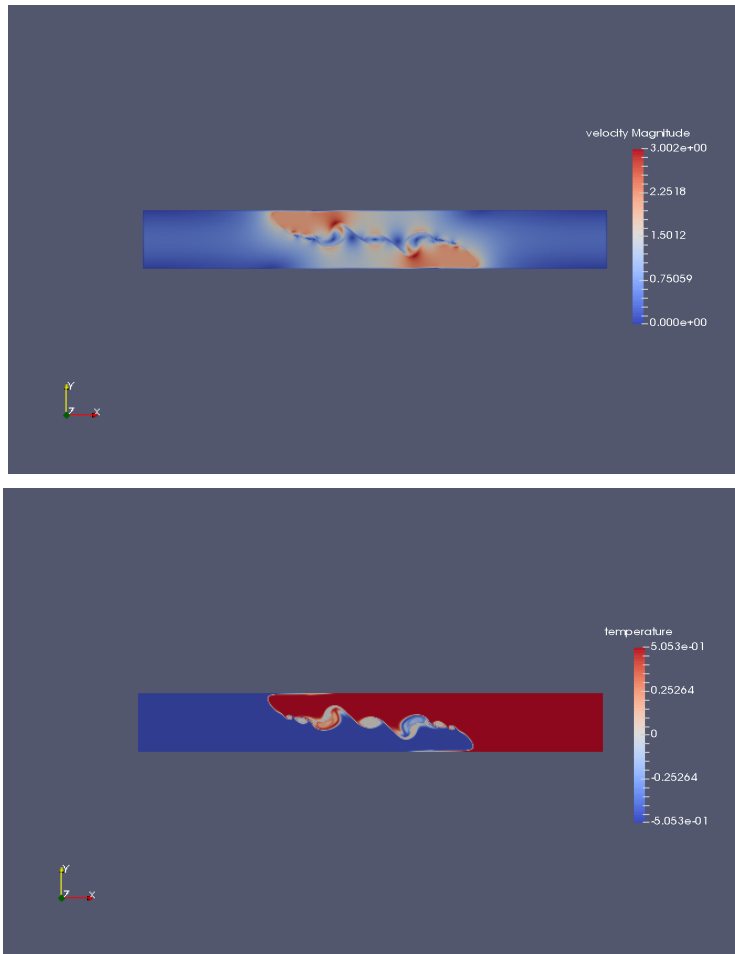
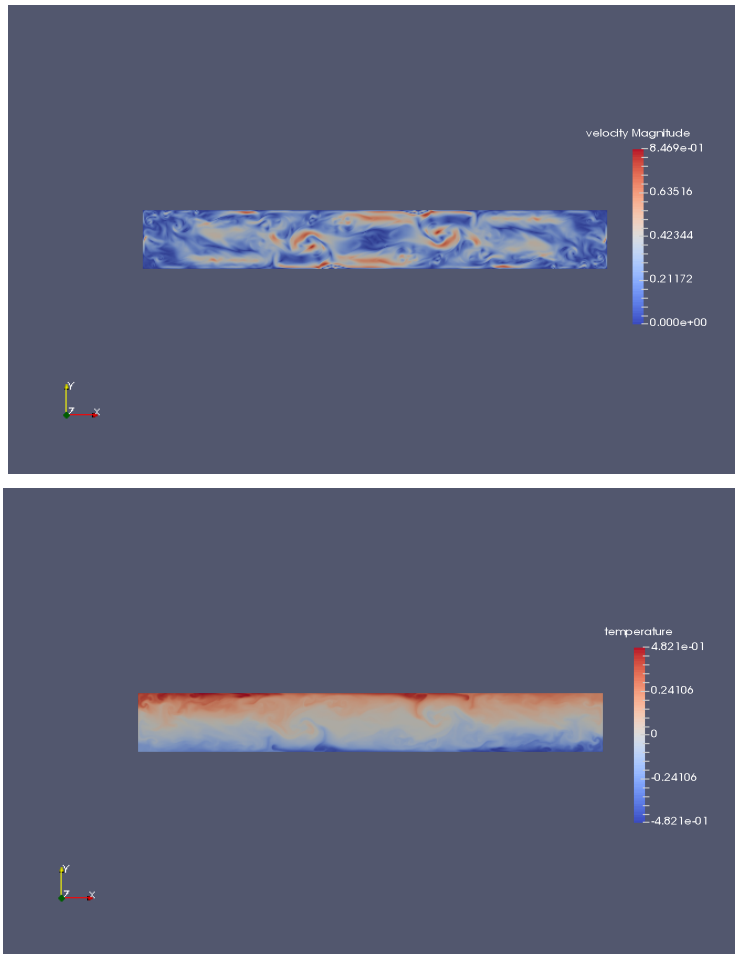Figure 15: Case two: Re = 8800: True solution profile at $t = 1$ (Top: velocity, Bottom: temperature)

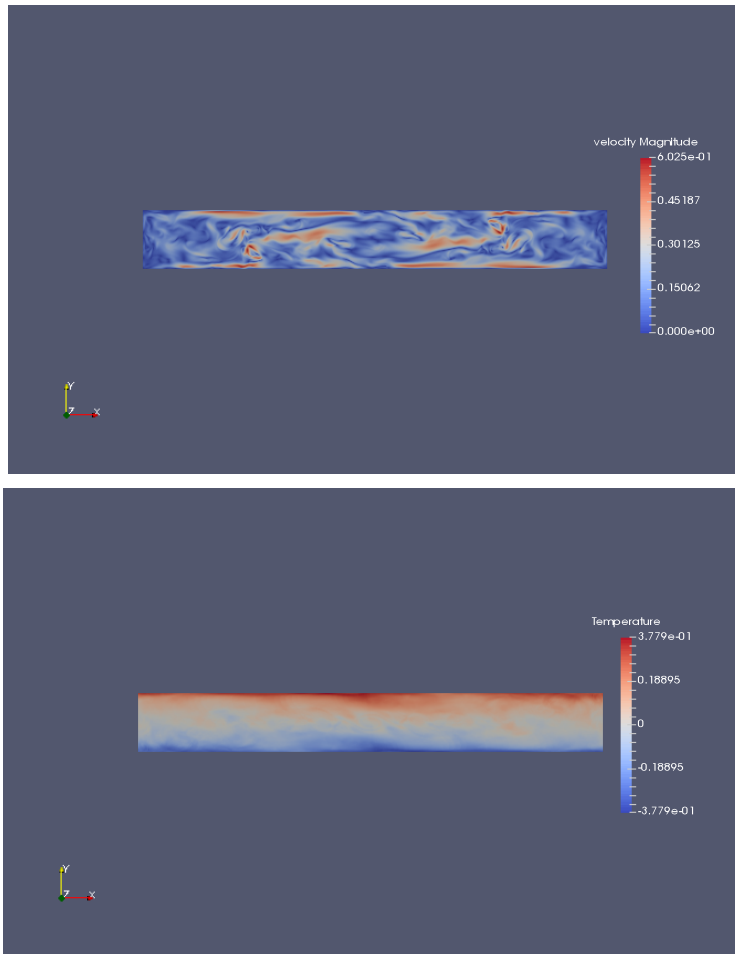Figure 16: Case two: Re = 8800: True solution profile at $t = 10$ (Top: velocity, Bottom: temperature)

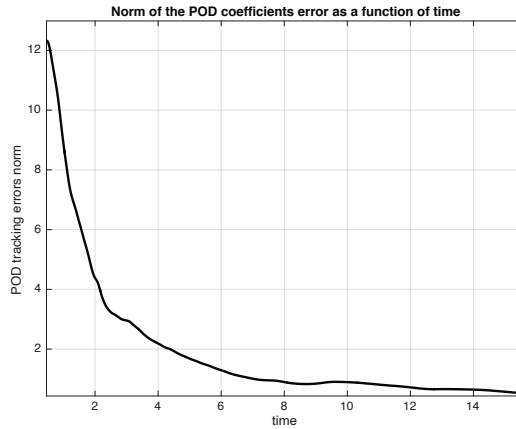Figure 17: Case two: Re = 8800: True solution profile at $t = 14.4$ (Top: velocity, Bottom: temperature)

Figure 18: $\|e\|_{\hat{\mathcal{H}}}$ as function of time- nominal case with $k = 0$

observer with the same nominal gain value $k = -10^5$, used in the previous tests (Nominal case). Using the same nominal gain value allows us to test the performance of the same observer, used in the nominal case, without adjustment or learning of a new gain, and see if there is indeed a need of an online learning step to improve the overall performance of the observer.

Let us first report in Figure 27 the norm of the error in the PODs coefficients estimation. We can see that the error norm decreases rapidly from its initial value of 10.54 to 2 but then remains in an oscillatory pattern around 2. At this point, we conjecture that this relatively bad estimation performance, comparatively to the nominal performance seen in Figure 19, is caused by this parametric uncertainty. We will come back to this statement later, and test if we can improve this performance by adjusting the observer's gain for this specific value of uncertainty. Next, we report in Figures 28- Top, and Figure 28- Bottom, the

36
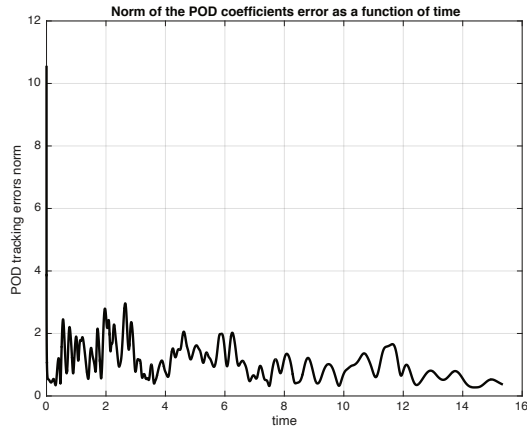
Figure 19: $\|e\|_{\hat{\mathcal{H}}}$ as function of time- nominal case with $k = -10^5$

first four POD coefficients' estimate of velocity and temperature, respectively. We can see that the estimated coefficients of temperature converge to the true coefficients rapidly, however, the velocity estimated coefficients converge to the true ones but remain oscillatory around the mean true values, as seen in the PODs estimation error norm result described earlier. As explained in the nominal case, these oscillations are partly due to the noisy output measurements[7], but in this uncertain case, the amplitude of these residual oscillations are higher than in the nominal case, which is due to the parametric uncertainty which is causing a bigger mismatch between the model used to design the observer and the true flow measurements. To improve this performance, we want to learn a more optimal observer gain, for this specific value of uncertainty. We do not

---

[7]We recall here that to simulate a more realistic scenario, we added bounded measurement noise in the form of random additive disturbances of maximum value 10^{-3}.
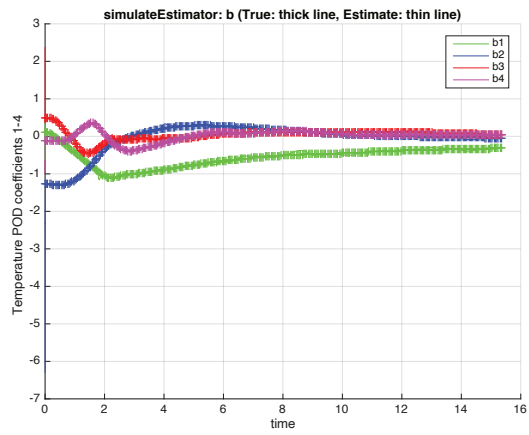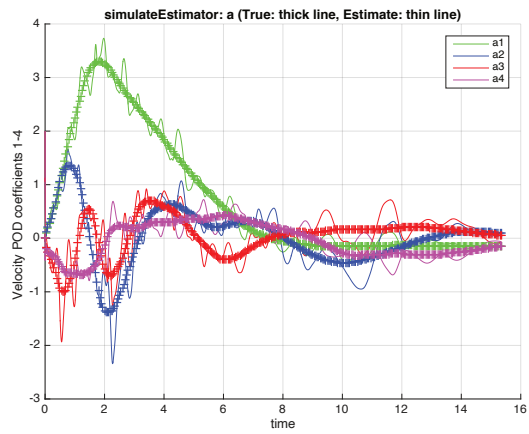
Figure 20: Estimated vs. actual POD coefficients over time- nominal case with $k = -10^5$ (Top: velocity PODs, Bottom: temperature PODs)
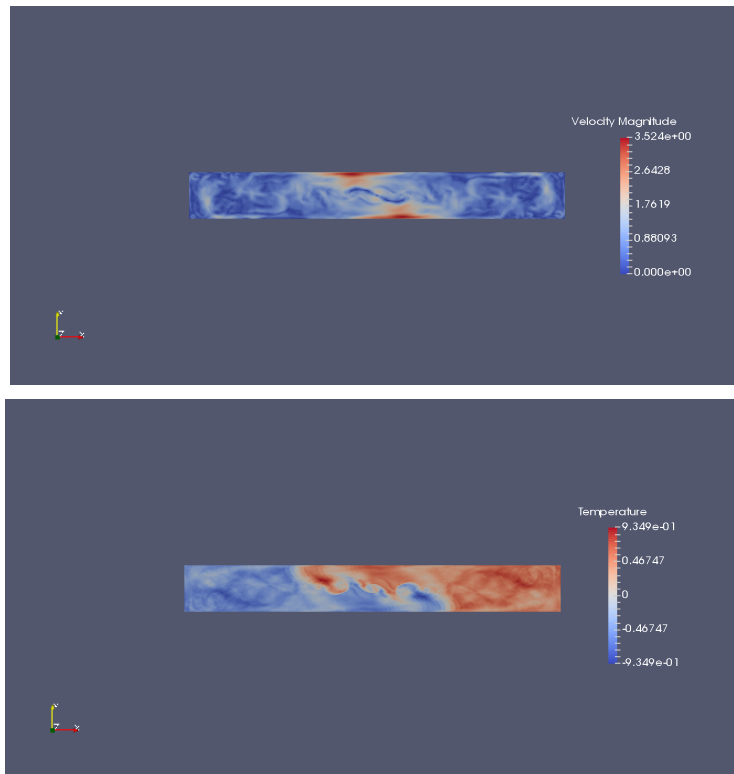
Figure 21: Estimated solution profile at $t = 1$- nominal case with $k = -10^5$
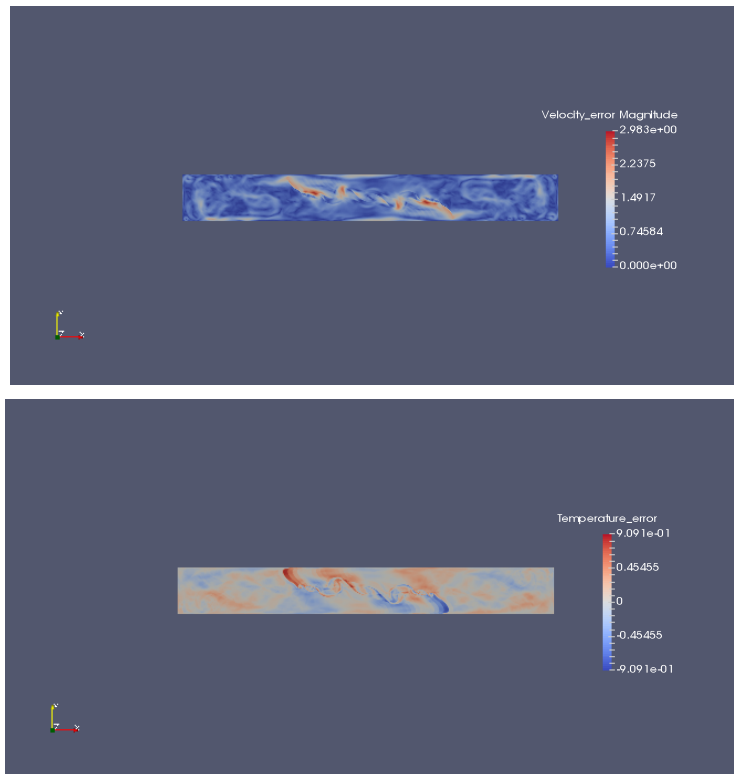(Top: velocity, Bottom: temperature)

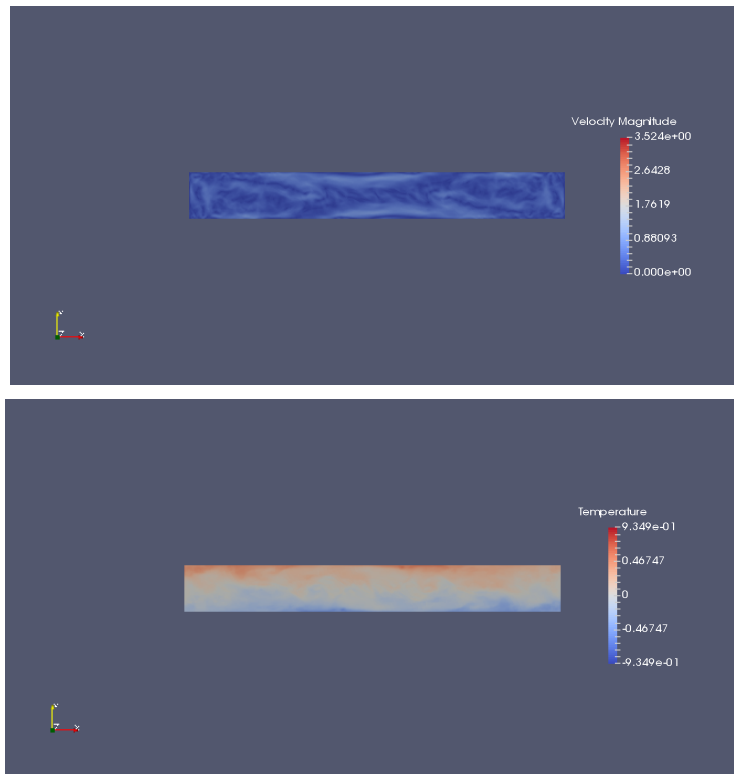Figure 22: Estimated error profile at $t = 1$- nominal case with $k = -10^5$ (Top: velocity, Bottom: temperature)
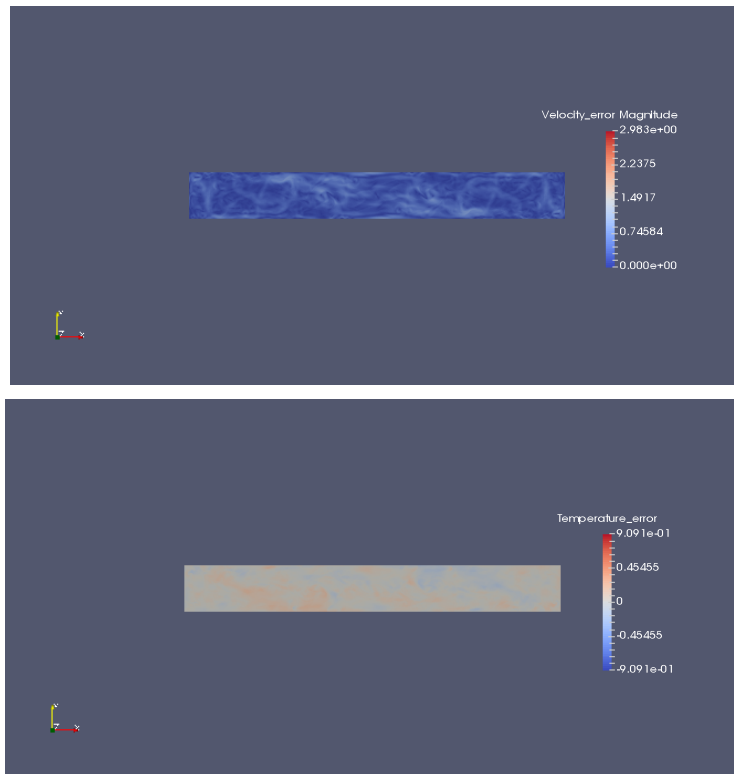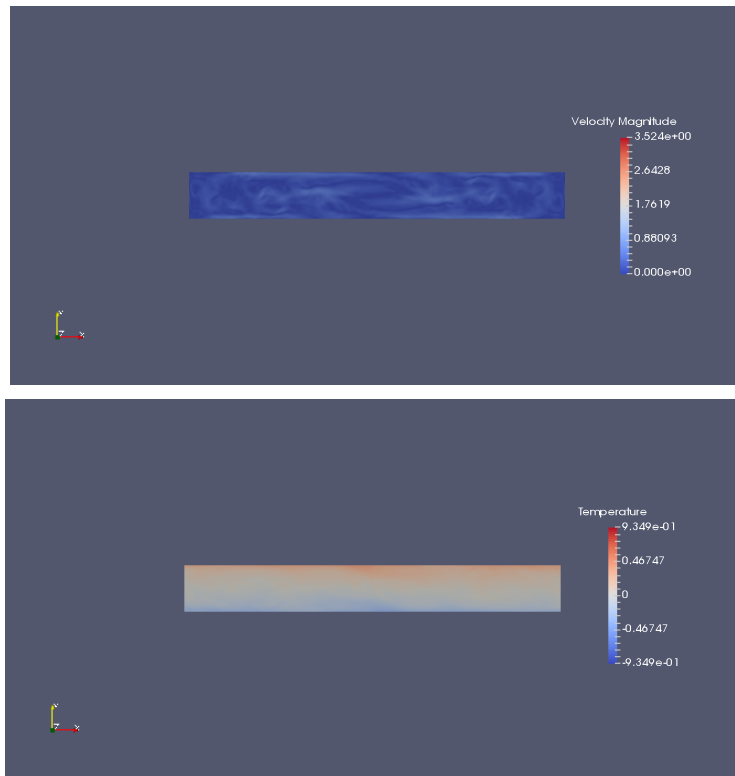
Figure 23: Estimated profile at $t = 10$- nominal case with $k = -10^5$ (Top: velocity, Bottom: temperature)

Figure 24: Estimated error profile at $t = 10$ - nominal case with $k = -10^5$ (Top: velocity, Bottom: temperature)

Figure 25: Estimated solution profile at $t = 14.4$- nominal case with $k = -10^5$
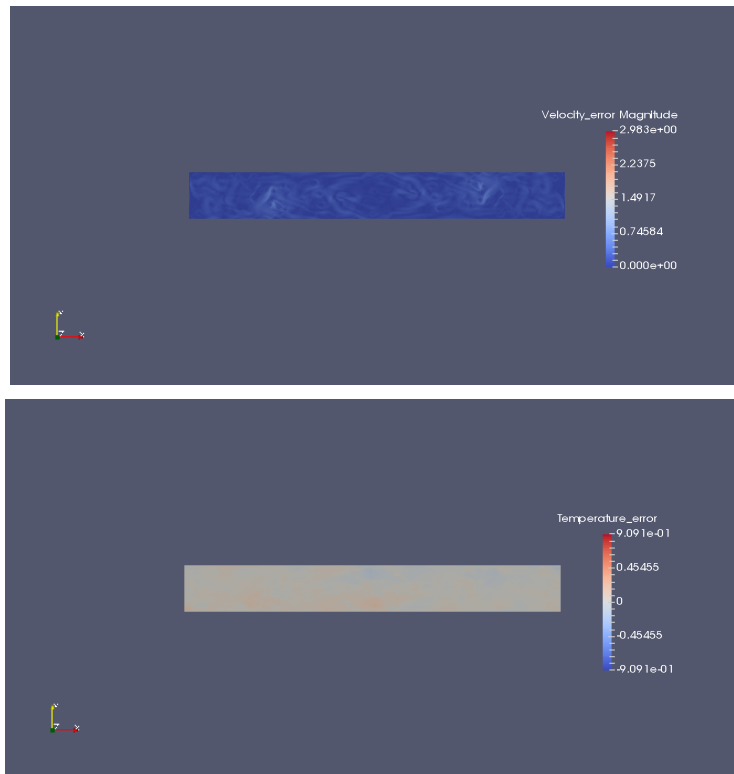(Top: velocity, Bottom: temperature)

Figure 26: Estimated error profile at $t = 14.4$-nominal case with $k = -10^5$ (Top: velocity, Bottom: temperature)

know if such gain exists, so we start by checking how does the learning cost function (26) vary as a function of the observer gain in this case. We show in Figure 29 the plot of this output-based learning cost as function of the gain. It is clear that the nominal value of the gain 10^5 is not optimal, since in this case, the learning cost is smaller for lower gain values, and reaches a minimal value for gains between -2.10^3 and -10^3. To check that this improvement in output tracking performance translates indeed to an improvement of the whole state estimate, and thus to the full velocity and temperature estimates, we plotted in Figure 30 this learning cost for the whole state vector, i.e., by substituting C in (26) with the identify matrix. We can see that the optimal region of estimation gains in this case is similar to the one for the output-based learning cost, which means that using the output-based learning cost in the extremum seeking algorithm, to learn an optimal estimation gain online, will lead to an improvement of the estimation performance for the full state vector.

Next, we report the results of the extremum seeking based online learning of the observer gain. Indeed, we have implemented the learning algorithm (26), (27), and (28) with the coefficients: $\omega_k = 100$, $\delta_k = 20$, $\epsilon_k = 10^{-3}$, and $a_k(0) = 5 \times 10^3$. We report in Figures 31, 32 the learning results. We can see in Figure 31 that the learning cost is minimized over the learning iterations. The learning cost starts from about 215, which corresponds to the initial gain value of 10^5, however, the learning cost decreases over the learning iterations, to reach a near optimal value of 114, which corresponds to the gain value of 1700, Figure 33. Note that we stopped the learning iterations at 150 since the performance optimization trend was clear, but one can use more iterations to fine-tune the final value closer to the true optimum seen in Figure 29. Finally, for comparison purposes, we show in Figure 34 the POD coefficients tracking error norm. We can see the improvement of the tracking performance in comparison with the results obtained for $k = -10^5$ depicted in Figure 27.
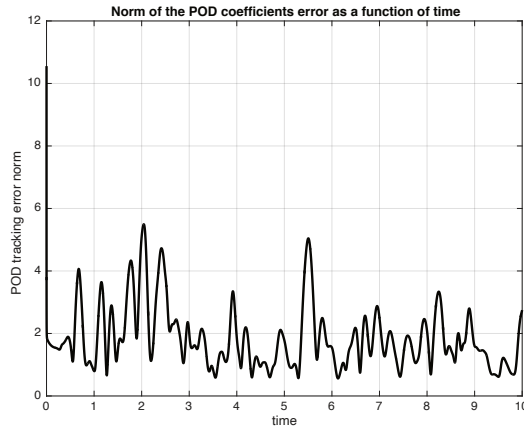
45

Figure 27: $\|e\|_{\hat{\mathcal{H}}}$ as function of time- uncertain case with $k = -10^5$

5   Conclusion

In this work we have proposed a POD-based reduced order model observer for the uncertain 2D Boussinesq equations. The observer includes the POD-based projection operator explicitly in its design. We then robustify this nominal observer against additive bounded structured uncertainties using nonlinear robust control tools. Finally, we add a layer of data-driven, realtime auto-tuning of the observer gain, using an extremum seeking approach. The performance of the observer is demonstrated on a challenging 2D Boussinesq test-case of unsteady lock-exchange flow problem with uncertain Reynolds numbers. The results of this work are encouraging and motivate us to pursue estimation for 3D Boussinesq equations for which high Reynolds numbers translate directly to physical turbulent flows, as well as experimental validations for indoor airflow estimation.
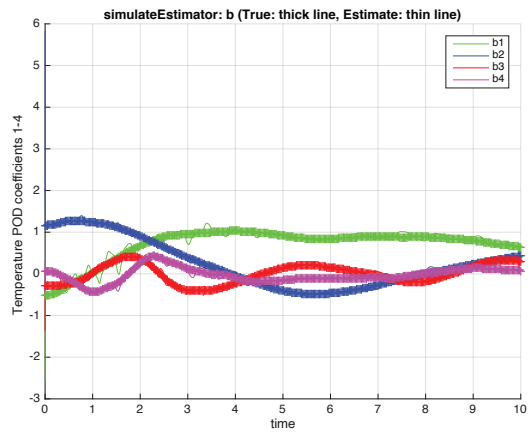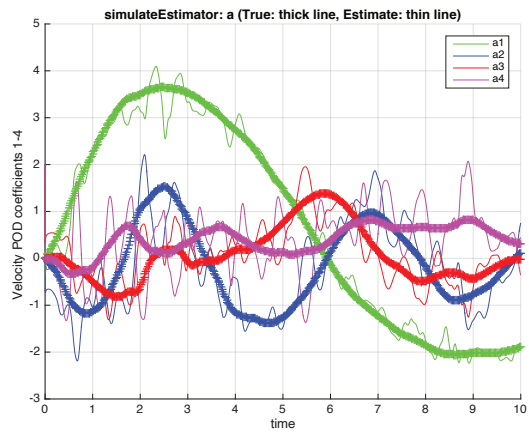
Figure 28: Estimated vs. actual POD coefficients over time- uncertain case with $k = -10^5$ (Top: velocity PODs, Bottom: temperature PODs)
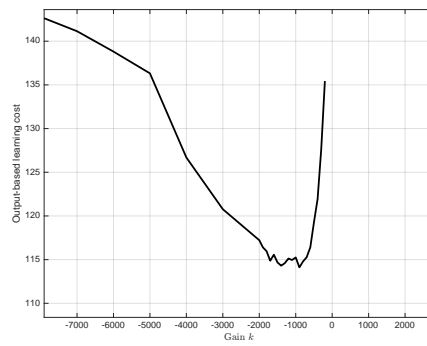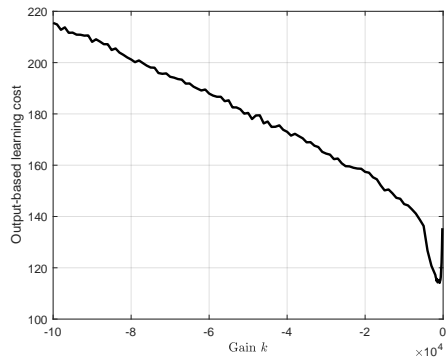
Figure 29: Learning cost as function of k: output-based (Top: full figure, Bottom: zoom at the optimal region)
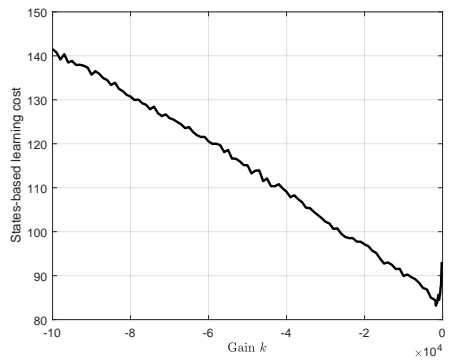
Figure 30: Learning cost as function of k: state-based

Another important open topic would be to study the effect of the type of basis function used for the observer design. For instance, it would be interesting to see if dynamical mode decomposition (DMD) could be used in this framework.
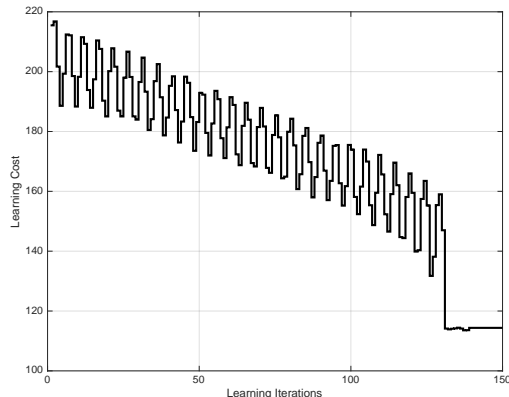
Figure 31: Learning cost as function of learning iterations

Appendix

Remark 1 [1]: We want to underline here that in applications, and due to the finite number of sensors (even sparse in most real-life applications), it is clear that equation (18), which stems from our POD formulation of the observer, constitutes an approximation in a least-squares sense of the exact condition (8) This is due to the fact that the pseudo-inverse $C^\dagger$ is only an approximation of the exact left-inverse of C, e.g. ([15], pp. 451-452). This approximation could also be obtained by directly minimizing the term $[A_c\mathcal{T} - \mathcal{T}A + FC]z$ for $z \in \text{span}\{\phi_i\}$, i.e., along a simulated solution of the system. Another solution would be to use the matrices decomposition used in [16] for solving a similar Sylvester equation (in the ODE setting). However, such solution will also be an approximation in our case of a non-square measurement operator C, i.e., less sensors than the large state variables number obtained from discretization. In essence, what we need is for the term $[A_c\mathcal{T} - \mathcal{T}A + FC]\,z(t)$ to be as small as achievable, under the constraint of finite number of sensors. Indeed, the
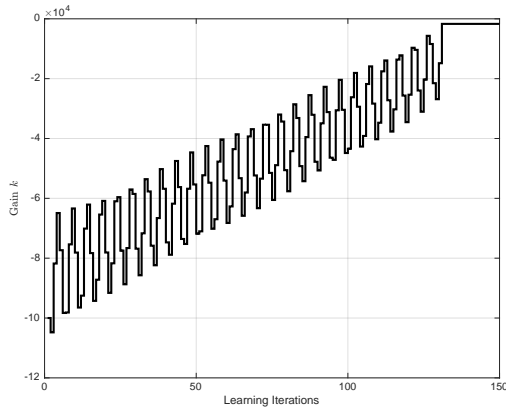
Figure 32: Gain learning as function of learning iterations

fact that condition (8) is not exactly satisfied does not change the exponential convergence of the error, since if we denote by $\text{res}_{Sylvester}$ the residual error in solving the Sylvester equation $A_c\mathcal{T} - \mathcal{T}A + FC = 0$, using (18), then due to Assumption 1, one can bound the norm of the residual term $\text{res}_{Sylvester}z$, which can then be included in the constant term β. Additionally, the effect of this bounded residual term can be compensated for by the robustification of the observer, as presented in the next section.

Remark 2 [1]: In practice, we can control the projection error $\mathcal{P}(\mathcal{T}, z)$ by suitable selection of the trajectory data and choosing enough basis functions r. However, we want to underline here the fact that the existence of such a basis function with clear dominant modes is only ensured for some PDEs that we denote here as *spectral PDEs*. In the case where such basis functions do not exist, e.g. hyperbolic PDEs, one could use recent results that propose more appropriate basis functions, e.g., [2, 31, 32].
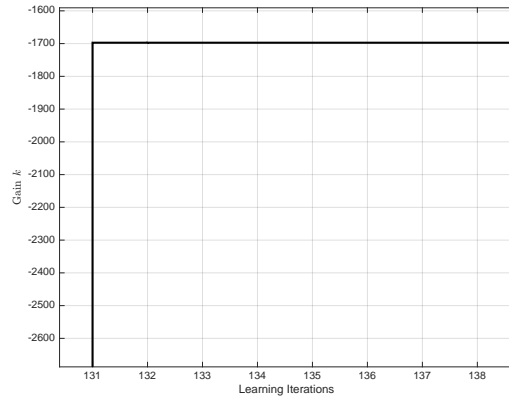
Figure 33: Gain learning as function of learning iterations- Zoom

References

[1] Benosman, M. and Borggaard, J. (2019), "Robust nonlinear state estimation for a class of infinite-dimensional systems using reduced-order models," *Int. Journal of Control*, DOI:10.1080/00207179.2019.1645359, to appear.

[2] Borggaard, J., Hay, A., and Pelletier, D. (2007), "Interval-based reduced-order models for unsteady fluid flow," *International Journal of Numerical Analysis and Modeling*, 4:353–367.

[3] Guay, M. and Hariharan, N. (2009), Airflow velocity estimation in building systems. In *IEEE American Control Conference*, pp. 908–913.

[4] T. John, M. Guay, N. Hariharan, and S. Narayanan (2010), POD-based observer for estimation in Navier–Stokes flow. *Computers & Chemical Engineering*, 34(6):965–975.
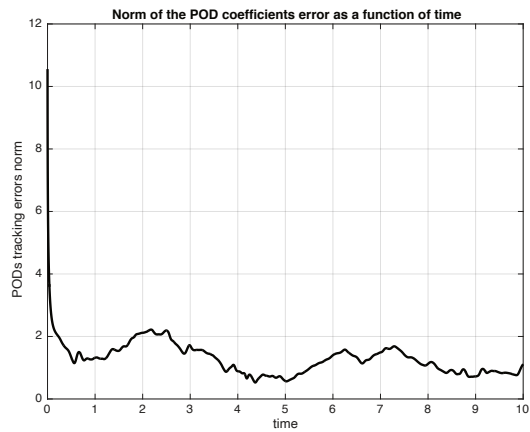
Norm of the POD coefficients error as a function of time

Figure 34: $\|e\|_{\hat{\mathcal{H}}}$ as function of time- uncertain case with $k = -1700$

[5] Reyhanoglu, M., MacKunis, W., Drakunov, S. V., and Ukeiley, L. (2011), Nonlinear estimation of fluid flow velocity fields. In *IEEE Conference on Decision and Control*, pp. 6931–6935.

[6] He, X., Hu, W., and Zhang, Y. (2018), Observer-based feedback boundary stabilization of the Navier-Stokes equations *Computer Methods in Applied Mechanics and Engineering*, 339:542–566.

[7] Nair, N. J. and Goza, A. (2020), Leveraging reduced-order models for state estimation using deep learning *Journal of Fluid Mechanics*, 897 R1:1–13.

[8] Smyshlyaev, A. and Krstic, M. (2010), "Adaptive Control of Parabolic PDEs," Princeton University Press.

[9] Borggaard, J., Gugercin, S., and Zietsman, L. (2014), "Compensators via H$_2$-based Model Reduction and Proper Orthogonal Decomposition," in *Proceedings of the 19th IFAC World Congress*, South Africa, Cape Town, pp. 7779–7784.

[10] Feng, H., and Guo, B.Z. (2017), "New unknown input observer and output feedback stabilization for uncertain heat equation," *Automatica*, 86:1–10.

[11] Hu, W., Singler, J. R., and Zhang, Y. (2016), "Feedback Control of a Thermal Fluid Based on a Reduced Order Observer," in *10th IFAC Symposium on Nonlinear Control Systems NOLCOS*, Monterey, California, pp. 116–121.

[12] Koga, S., Benosman, M., and Borggaard, J. (2019), "Learning-Based Robust Observer Design for Coupled Thermal and Fluid Systems," in *IEEE American Control Conference*, to appear.

[13] Holmes, P., Lumley, J.L., and Berkooz, G. (1998), *Turbulence, coherent structures, dynamical systems and symmetry*, Cambridge University Press.

[14] Kunisch, K., and Volkwein, S. (2007), "Galerkin proper orthogonal decomposition methods for a general equation in fluid dynamics," *SIAM Journal on Numerical Analysis*, 40:492–515.

[15] Beutler. F. J., (1965), "The Operator Theory of the Pseudo-Inverse. I. Bounded Operators," *Journal of Mathematical Analysis and Applications*, 10:451–470.

[16] Witczak, M., Buciakowski, M., Puig, V., Rotondo, D., and Nejjari, F. (2016), "An LMI approach to robust fault estimation for a class of nonlinear systems," *International Journal of Robust and Nonlinear Control*, 26:1530–1548.

[17] Hjalmarsson, H. (1998), "Control of nonlinear systems using iterative feedback tuning," in *IEEE, Conference on Decision and Control*, pp. 2083–2087.

[18] Lequin, O., Gevers, M., Mossberg, M., Bosmans, E., and Triest, L. (2003), "Iterative feedback tuning of PID parameters: comparison with classical tuning rules," *Control Engineering Practice*, 11:1023–1033.

[19] Hjalmarsson, H. (2002), "Iterative feedback tuning-an overview," *International Journal of Adaptive Control and Signal Processing*, 16:373–395.

[20] Benosman, M. (2016), "Multi-Parametric Extremum Seeking-based Auto-Tuning for Robust Input-Output Linearization Control," *Int. Journal of Robust and Nonlinear Control*, 26:4035–4055.

[21] Killingsworth, N.J., and Krstic, M. (2006), "PID tuning using extremum seeking," *IEEE Control Systems Magazine*, pp. 1429–1439.

[22] Tan, Y., Nesic, D., Mareels, I., and Astolfi, A. (2009), "On global extremum seeking in the presence of local extrema," *Automatica*, pp. 245–251.

[23] Benosman, M., Borggaard, J., San, O., and Kramer, B. (2017), "Learning-based robust stabilization for reduced-order models of 2D and 3D Boussinesq equationsl," *Applied Mathematical Modelling*, 49:162–181.

[24] Du, J., Fang, F., Pain, C.C., Navon, I.M., Zhu, J., and Ham, D.A. (2013), "POD reduced-order unstructured mesh modeling applied to 2D and 3D fluid flow," *Computers and Mathematics with Applications*, 65:362–379.

[25] San, O. and Borggaard, J. (2014), "Basis Selection and Closure for POD Models of Convection Dominated Boussinesq Flows," *Proceedings of the 21st International Symposium on Mathematical Theory of Networks and Systems*, Groningen, The Netherlands.

[26] San, O. and Borggaard, J. (2015), "Principal interval decomposition framework for POD reduced-order modeling of convective Boussinesq flows," *International Journal for Numerical Methods in Fluids*, 78:37–62.

[27] Gunzburger, M. (1989), *Finite Element Methods for Viscous Incompressible Flows: A Guide to Theory, Practice, and Algorithms*, Academic Press.

[28] Badra, M. (2012), "Abstract settings for the stabilization of nonlinear parabolic system with a Riccati-based strategy. Application to Navier-Stokes and Boussinesq equations with Neumann or Dirichlet control," *Discrete and Continuous Dynamical Systems–Series A*, 252(9):5042–5075.

[29] Drmac, Z. and Gugercin, S. (2016), A new selection operator for the discrete empirical interpolation method—improved a priori error bound and extensions. *Methods and Algorithms for Scientific Computing*, 32(8):631–648.

[30] de Wilde, P., Tian, W., and Augenbroe, G. (2011), "Longitudinal prediction of the operational energy use of buildings," *Building and Environment*, 46:1670–1680.

[31] Balajewicz, M.J., Dowell, E.H., and Noack, B.R. (2013), "Low-dimensional modelling of high-Reynolds-number shear flows incorporating constraints from the Navier-Stokes equation," *Journal of Fluid Mechanics*, 729, 285–308.

[32] Rim, D., and Mandli, K.T. (2018), "Model reduction of a parametrized scalar hyperbolic conservation law using displacement interpolation," *arXiv:1805.05938 [math.NA]*.